From the Department of Clinical Neuroscience
Karolinska Institutet, Stockholm, Sweden

PENUMBRA OXYGEN METABOLISM AND ACUTE NEUROINFLAMMATION IN ISCHEMIC STROKE

MRI and PET imaging of a M2 Occlusion Model in Rat

Philip Little

Karolinska Institutet

Stockholm 2020

Published by Karolinska Institutet.
Printed by Arkitektkopia AB, 2020
Cover art: R2* MRI image collected during M2CAO. The image has been optimized for publication.

ISBN **978-91-7831-750-9**

Penumbra Oxygen Metabolism and Acute Neuroinflammation in Ischemic Stroke

MRI and PET imaging of a M2 Occlusion Model in Rat

THESIS FOR DOCTORAL DEGREE (Ph.D.)

The thesis will be defended on the 27th of March 2020.

By

Philip Viktor Little

Principal Supervisor:

Staffan Holmin
Karolinska Institutet
Department of Clinical Neuroscience
Division of Neuroradiology

Co-supervisors:

Peter Damberg
Karolinska Institutet
Department of Clinical Science, Intervention
and Technology

Michael Söderman
Karolinska Institutet
Department of Clinical Neuroscience
Division of Neuroradiology

Tommy Andersson
Karolinska Institutet
Department of Clinical Neuroscience
Division of Neuroradiology

Opponent:

Leif Østergaard
Aarhus University, Denmark
Department of Clinical Medicine
Department of Radiology
Center of Functionally Integrative Neuroscience

Examination Board:

Johan Wassélius
Lund University
Department of Diagnostic Radiology
Stroke Imaging Research Group

Zaal Kokaia
Lund University
Department of Neurology
Lund Stem Cell Center

Anders Lewén
Uppsala University
Department of Neuroscience
Division of Neurosurgery

To family, friends and home

Nevertheless, I long - I pine, all my days –
to travel home and see the dawn of my return.
And if a god will wreck me yet again on the wine-dark sea,
I can bear that too, with a spirit tempered to endure.
Much have I suffered, labored long and hard by now
in the waves and wars. Add this to the total –
bring the trial on!

- Homer, *the Odyssey*

ABSTRACT

Acute ischemic stroke (AIS) is caused by the sudden occlusion of a major artery of the brain, and results in infarction and severe ischemia within affected brain regions. If ischemic regions are rapidly revascularized, the neurological disability resulting from AIS can be significantly reduced. Accordingly, endovascular thrombectomy aims to restore blood flow to ischemic tissue-at-risk, penumbra, that remains viable in the short-term by virtue of collateral blood flow and an increased extraction of oxygen (OEF) from the blood.

Diagnostic imaging is an essential component in the identification of patients who are suitable for revasculatory treatment. The aim of this thesis was to investigate AIS pathophysiology, with a special focus on oxygen metabolism and neuroinflammation, and subsequently to develop and improve methods for the identification of penumbra tissue through imaging with magnetic resonance imaging (MRI) and positron emission tomography (PET). To achieve this, we used a middle cerebral artery M2-segment occlusion model in rat that had previously been designed to increase the translational potential of experimental AIS research (M2CAO).

In **paper I** we employed the PET tracer [^{11}C]PBR28 to longitudinally profile the neuroinflammatory response during the first 14 days following transient M2CAO. We complemented PET examinations with ex-vivo immunohistochemistry (IHC). Results validated [^{11}C]PBR28 and revealed early microglial activation and glial scar formation following M2CAO. In **paper II**, we used diffusion- and perfusion weighted MRI (DWI, PWI) to outline the emergence and expansion of ischemic injury at the expense of the penumbra during AIS. We used the established DWI/PWI mismatch concept as a surrogate of the penumbra. Results showed that although the initial spread of ischemic injury is rapid, not all tissue contained in the DWI/PWI mismatch is at risk of infarction. In **paper III**, we assembled a blood oxygen level dependent MRI protocol which was combined with PWI. The protocol was used to approximate regional tissue OEF during M2CAO and after blood flow had been restored. When combined with DWI, oxygen metabolism MRI achieved an improved penumbra specificity when compared to the DWI/PWI mismatch protocol used in paper II. In **paper IV**, we compared PET tracers [^{18}F]FMISO and [^{64}Cu]CuATSM in identifying tissue hypoxia resulting from M2CAO, and investigated the effects of hypoxia on ischemic tissue using IHC analysis. [^{18}F]FMISO was superior to [^{64}Cu]CuATSM in identifying tissue hypoxia. In conclusion, the imaging methodologies investigated in this study have high diagnostic potential in AIS as well as in cases of chronic cerebral hypoperfusion.

LIST OF SCIENTIFIC PAPERS

I. Acute neuroinflammation in a clinically relevant focal cortical ischemic stroke model in rat: longitudinal positron emission tomography and immunofluorescent tracking
Mikós Tóth*, **Philip Little***, Fabian Arnberg, Jenny Häggkvist, Jan Mulder, Christer Halldin, Balázs Gulyás and Staffan Holmin
Brain Structure and Function (2015).
***Authors contributed equally**

II. Preserved Collateral Blood Flow in the Endovascular M2CAO Model Allows for Clinically Relevant Profiling of Injury Progression in Acute Ischemic Stroke
Philip Little, Ola Kvist, Rikard Grankvist, Stefan Jonsson, Michael Söderman, Fabian Arnberg and Staffan Holmin
PLoS One (2017)

III. Oxygen Metabolism MRI - A Comparison with Perfusion Imaging in a Rat Model of MCA Branch Occlusion and Reperfusion
Philip Little, Sandra Kraft, Arvin Chireh, Peter Damberg and Staffan Holmin
Journal of Cerebral Blood Flow and Metabolism (2019)

IV. Cellular Hypoxia in Clinically Relevant Stroke model – A comparison of [^{18}F]FMISO and [^{64}Cu]CuATSM PET-tracers
Philip Little, Fabian Arnberg, Emma Jussing, Andreas Ingemann Jensen, Nicholas Mitsios, Jan Mulder, Thuy Tran and Staffan Holmin
Submitted and undergoing revision

Additional Contributions

I. Imaging of a clinically relevant stroke model: glucose hypermetabolism revisited.
Fabian Arnberg, Jonas Grafström, Johan Lundberg, Sahar Nikkhou-Aski**, Philip Little**, Peter Damberg, Nicholas Mitsios, Jan Mulder, Li Lu, Michael Söderman, Sharon Stone-Elander and Staffan Holmin
Stroke (2015)

II. Superselective endovascular tissue access using trans-vessel wall technique: feasibility study for treatment applications in heart, pancreas and kidney in swine
Rikard Grankvist, Mats Jensen-Urstad, Jonathan Clarke, Miia Lehtinen, **Philip Little**, Johan Lundberg, Fabian Arnberg, Kenneth Chien, Staffan Holmin
Journal of Internal Medicine (2019)

LIST OF ABBREVIATIONS

[^{11}C]-FMZ	-	^{11}C-Flumazenil (PET tracer)
[^{11}C]PBR28	-	^{11}C-Peripheral benzodiazepine receptor (PET tracer)
[^{18}F]FMISO	-	^{18}F-Fluoromisonidazol (PET tracer)
[^{64}Cu]CuATSM	-	^{64}Cu-diacetyl-bis(N4- methylthiosemicarbazone) (PET tracer)
%SUV	-	Standardized uptake value
ACA	-	Anterior cerebral artery
ADC	-	Apparent Diffusion Coefficient
AIS	-	Acute Ischemic Stroke
ANOVA	-	Analysis of variance
ASL	-	Arterial spin labeling
ATP	-	Adenosine triphosphate
B_0	-	Magnetic Field generated by a MRI-scanner
BOLD	-	Blood oxygen level dependent (imaging)
C^{15}O	-	^{15}O-labeled carbon monoxide
C$^{15}O_2$	-	^{15}O-labeled carbon dioxide
CBF	-	Cerebral blood flow
CBV	-	Cerebral blood volume
CCH	-	Chronic cerebral hypoperfusion
$CMRO_2$	-	Cerebral metabolic rate of oxygen
CPP	-	Cerebral perfusion pressure
CT	-	Computerized tomography
DASL	-	Dynamic ASL
dHb	-	Deoxygenated hemoglobin
DWI	-	Diffusion weighted imaging
ECA	-	External carotid artery
FOV	-	Field of view
GE	-	Gradient echo (MRI)
GFAP	-	Glial fibrillary acidic protein
H_2^{15}O	-	^{15}O-labeled water
Hct	-	Hematocrit (stor bokstav)
LMAs	-	Leptomeningeal anastomoses
M2CAO	-	Middle cerebral artery M2-segment occlusion model
MAB	-	Monoclonal antibody

MCA	-	Middle cerebral artery
MCAO	-	Middle cerebral artery suture occlusion model
MEMS	-	Multi echo multi slice (MRI sequence)
MGE3D	-	Multi gradient echo 3D (MRI sequence)
MRI	-	Magnetic Resonance Imaging
MTT	-	Mean transit time
NeuN	-	Neuronal Nuclei
OEF	-	Oxygen Extraction Fraction
PBR	-	Peripheral benzodiazepine receptor
PCA	-	Posterior cerebral artery
Pcom	-	Posterior communicating artery
PET	-	Positron emission tomography
PWI	-	Perfusion weighted imaging
RF	-	Radiofrequency
ROI	-	Region of interest
SD	-	Sprague-Dawley rat strain
SE	-	Spin echo (MRI)
SNR	-	Signal-to-noise
T-DASL	-	Turbo dynamic ASL
T1WI	-	T1-weighted imaging
T2WI	-	T2-weighted imaging
TSA	-	Tyramidine signal amplification
TSPO	-	Translocator protein 18 kDa

CONTENTS

1. BACKGROUND

Acute ischemic stroke (AIS) is a leading cause of death and neurological disability worldwide(*1*). A sudden occlusion of a large brain vessel will result in the rapid infarction of affected tissue within the so-called ischemic core. In the following hours, irreversible damage will appear in the surrounding tissue-at-risk, referred to as ischemic penumbra, unless blood flow is restored(*2*). The acute revascularisation of salvageable tissue-at-risk accordingly remains the long-standing therapeutic target in AIS, with neuroimaging serving as the foremost diagnostic instrument(*3, 4*). The therapeutic aim is to stem the spread of infarction within the ischemic penumbra, which are regions that have not yet suffered irreversible damage, and where an increased oxygen extraction fraction (OEF) from blood to brain tissue sustains tissue viability in the short-term(*5*). The aim of diagnostic imaging is to achieve examinations with a high sensitivity and specificity for penumbra, but that are still practical enough to be clinically applicable. In 2015, a series randomized trials showed the benefits of endovascular mechanical thrombectomy in the first hours after stroke, when aided by diagnostic imaging(*6*). Since then, other studies have produced evidence of prolonged penumbra viability in a proportion of AIS cases(*7, 8*), thereby increasing the demand on imaging techniques to achieve high penumbra specificity in order to enable clinicians to proceed with revasculatory interventions also in these patients. There is also an increasing interest in improving diagnostic imaging of patients presenting with symptoms potentially caused by subacute to chronic cerebral hypoperfusion (CCH)(*9*), a condition associated with neurodegenerative disorders and dementia. While AIS is caused by a sudden and dramatic loss tissue perfusion, the less severe but unremitting condition of CCH likewise results in an inadequate supply of glucose and oxygen to affected brain regions. As in AIS, this impedes normal neurological function and may result in a regional increase in OEF in order to sustain cellular viability. The causes of CCH include CBF-limiting pathologies of the cerebral vasculature which may be alleviated through mechanical thrombectomy. However, as in AIS, this requires diagnostic imaging capable of assisting the clinician with the information needed to assess whether to proceed with the revasculatory treatment. Neuroimaging is now capable of providing a large amount of different examinations, all with varying value for the process of diagnostic decision-making. Information on tissue status, perfusion, site of occlusion and collateral flow status(*10*) are routinely available using computerized tomography (CT) and magnetic resonance imaging (MRI). Blood oxygen level dependent (BOLD) techniques for MRI, and positron emission tomography (PET) tracers capable of identifying inflammation and hypoxia have the potential to improve the future of AIS- as well as CCH associated health care(*11*).

1.1 The ischemic penumbra

1.1.1 Time is brain

In 1981, Astrup and colleagues described the ischemic penumbra as functionally silent yet structurally intact brain tissue, lingering between the blood flow thresholds of electrical inactivity and irreversible damage(*12*). In AIS-associated health care, the expression "time is brain" (Figure 1) is used to emphasize the importance of rapid intervention and early restoration of blood flow (reperfusion) in order to salvage the penumbra(*13*). We now understand that the penumbra is kept viable in the short-term by metabolic adjustments(*14*) such as increased OEF, as well as by the recruitment of collateral vessels(*15*) which provide compensatory blood flow from unaffected arteries in the brain.

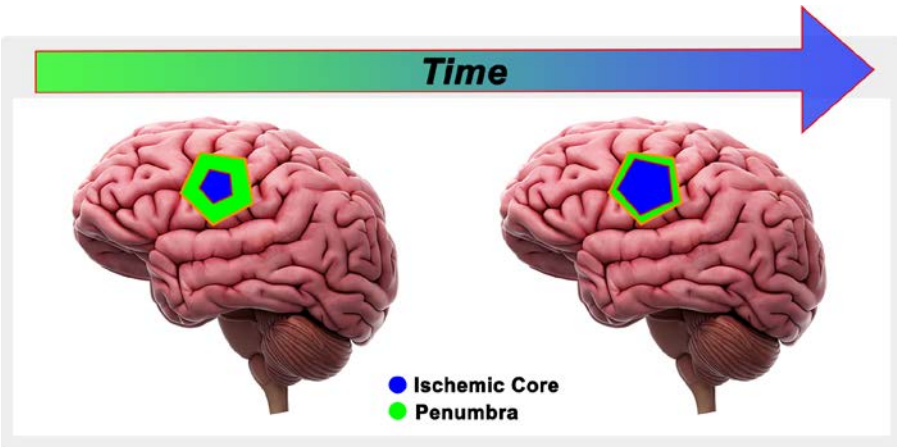

Figure 1. Time is brain. In acute ischemic stroke, there is a continuous expansion of the irreversibly damaged ischemic core (blue). The tissue-at-risk, known as penumbra (green), will thereby succumb to infarction unless blood flow is restored in time.

1.1.2 Misery perfusion

Demands on the circulatory system to maintain a constant delivery of oxygenated blood to the brain are high, leaving neuronal tissue susceptible to injury and functional impairment in the case of a sudden drop in tissue perfusion. The healthy brain implements hemodynamic autoregulation in order to compensate for fluctuations in the mean arterial blood pressure. The autoregulatory mechanism is maintained by the continual dilation and constriction of the vascular bed, which allows cerebral regions to sustain a constant ratio between cerebral blood flow (CBF) and the metabolic requirements for oxygen and glucose(*16*).

Misery perfusion(*17*) is a term used to describe the pathophysiological state during which metabolic and hemodynamic changes are employed to compensate for an acute loss in cerebral perfusion pressure (CPP), as in the case of AIS or CCH. The initial reaction following a sudden loss of CPP is a rapid dilation of the vascular bed within affected regions, as well as of the leptomeningeal anastomoses (LMAs) that connect the distal cortical branches of the major arteries of the brain (*18-20*). The dilation of small arteries and arterioles increases the local cerebral blood volume (CBV) within affected areas, thereby raising the CBV/CBF ratio. This is equivalent to a decrease in the rate of large-vessel cerebral circulation and a corresponding increase in the mean transit time (MTT) of red blood cells through tissue (*16*). A substantial decrease in CBF and an increase in MTT will result in inadequate amounts of oxygen being supplied to the brain tissue, a pathological condition known as *ischemia*.

1.1.3 Increased OEF sustains the penumbra

The energy requirements of the human brain are sustained almost entirely by the oxidative metabolism of glucose. In total, approximately three quarters of the adenosine triphosphate (ATP) produced in neuronal tissue is expended to power processes necessary for neuronal function, with the remaining quarter allocated to cellular housekeeping(*21*). If CPP decreases beyond the vasodilatory capacity of the cerebral autoregulation this will result in ischemia. The resulting tissue damage is a product of both the severity and the duration of the perfusion deficit. A severe reduction to CBF levels of 12 – 22 ml/ 100 g/ min will cause ischemic damage if left unresolved, but may in the short term be compensated by metabolic adjustment. In order to sustain the cerebral metabolic rate of oxygen ($CMRO_2$) necessary for cell survival, the OEF of affected tissue regions becomes increased. Imaging modalities like PET and MRI have the potential to identify the ischemic penumbra by examining the oxygen metabolism of ischemic tissue. More specifically, a ~~ 40% increase OEF in conjunction with a sustained $CMRO_2$ has been proposed as a specific marker of the ischemic penumbra, and has been employed in imaging regimes designed with the aim of being able to identify tissue-at-risk (*5, 14, 22*).

1.2 Imaging modalities – Overview

1.2.1 Magnetic Resonance Imaging

MRI(*21, 22*) is an imaging modality routinely employed in research as well as in clinical practice. Like CT, MRI produces greyscale cross sectional images with high resolution. Unlike CT, PET and conventional X-ray, MRI does not produce ionizing radiation but instead use powerful magnetic fields to achieve high contrast images of soft tissue, fat and fluids.

MRI utilizes the abundance of hydrogen protons contained in the bodies of humans and animals. These protons have *spin,* which may be described as a continuous rotation around their own axes which produces localized magnetic moments. In their natural state, the magnetic moments within an object, such as the human body, are randomly arranged in a manner that maintains magnetic equilibrium. Magnetic moments maintain a processing motion around the any magnetic field that acts upon them. Precession occurs at a frequency (the Larmor frequency) which is defined by the gyromagnetic ratio and is proportional to the strength of the magnetic field. If subjected to the strong magnetic field (B_0) of a MRI scanner the direction of magnetic moments will become distributed in such a way that produces a net magnetization vector either parallel or anti-parallel to the direction of B_0. MRI utilizes the net magnetization vector by applying to it radiofrequency (RF) pulses precisely matching the Larmor frequency. When subjected to such RF pulses, protons will absorb energy and move to a higher state of energy, a process referred to as *excitation*. Excitation will push the net magnetization vector to leave the equilibrium and move, *flip*, into an angle (commonly 0-90 degrees) relative to B_0. In addition to flipping, the magnetic moments will begin to precess in a synchronized manner, achieving *phase-coherence.*

In order to enable MRI to specify the position of protons within the examined object, additional magnetic fields in the form of gradients are applied. The magnetic gradient will modify B_0 strength, thereby increasing the Larmor frequency of examined protons along the direction of the gradient. By tailoring the frequency of the RF pulse used for excitation to match the Larmor frequency, proton spins achieve precession coherence in one slice at the time, and the position of the examined protons along the gradient can be determined in in a process called slice-selection. Subsequently, more gradients are applied in perpendicular directions to the slice-select gradient. These gradients will affect the Larmor frequency, as well as the phase of the net magnetization precession. The net magnetization precession will induce a voltage in the receiver coil of the MRI. The voltage arising from individual voxels will be modulated accordingly to the effects on net magnetization precession by the applied gradients. The marginal changes to voltage produced by gradients can then be used to locate individual voxels in space.

Relaxation

Once the RF pulse used for excitation is discontinued, protons that have achieved a higher state of energy, including precession coherence, will inevitably return to a lower energy equilibrium. This process is referred to as *relaxation* and is made up by two distinct components; longitudinal and transverse relaxation which are used in T1- and T2- weighted imaging, respectively (T1WI, T2WI).

T1WI is used mainly to attain high contrast, anatomical images of soft tissue. During longitudinal process of T1-relaxation, the excess energy of the proton is dispersed into the surrounding molecular environment in which the proton is located. Large molecules, such as fat, will reestablish its net magnetization vector more rapidly than tissues made up by more mobile molecules, such as water. Accordingly, the longitudinal relaxation is faster in fat than in water, giving rise to a high signal in T1WI.

T2WI is routinely used to identify soft tissue pathology. T2WI is based on the process referred to as transverse relaxation. As with the longitudinal relaxation harnessed in T1WI, transverse relaxation is dependent on the size and properties of the molecules that make up the examined tissue. However, transverse relaxation is a different and independent process to longitudinal relaxation. As described above, the RF pulse used to move the net magnetization vector into a direction perpendicular to B_0 also results in precession phase coherence. Precession constitutes a transverse component of the net magnetization vector. The transverse magnetization vector will decay as its precession begins lose phase coherence. This occurs because protons become affected by microscopic inhomogeneities within the magnetic field.

1.2.2 Positron Emission Tomography

PET(*25, 26*) is an imaging modality capable of tracking disease-associated processes such as metabolism, hypoxia, inflammation as well as the distribution and kinetics of pharmaceuticals. PET employs radiotracers, which consist of probe molecules that have been attached to positron emitting radionuclides. Positrons are positively charged particles of comparable mass to electrons. A radionuclide is unstable form of a common element which emits radioactivity as it releases excess energy, a process referred to as decay. Commonly used radionuclides are ^{11}C (half-life: 20.3 min), ^{13}N (9.97 min), ^{15}O (124 s) and ^{18}F (110 min). The most used radiotracer by far is Fluorodeoxyglucose ($[^{18}F]FDG$), radioactive sugar, which is employed to examine tissue metabolism in several pathological condiitons.

Once injected into the circulation of a human or animal, the radiotracer will exhibit an affinity for specific sites onto which they undergo reversible or irreversible binding. The radionuclide component of the tracer undergoes a continuous decay during which positrons are emitted at high velocity. As the positron travels through tissue it interacts with and ionizes the biological material, resulting in a gradual decrease in velocity. Ultimately there occurs an interaction with an electron, commonly a short distance from the site of emission. The positron-electron interaction results in both particles being annihilated. The reaction produces two high energy photons (511 keV) which are immediately projected in opposite directions. These

photons are registered as pulses by a 360° detector ring surrounding the examined subject. Subsequently, coincidence analysis is performed based on the assumption that specific photons will have reached opposing detector elements within a timeframe of a few nanoseconds. By disregarding photons pulses which were not matched at the opposing element within this time frame, the approximate location of radioactive decay can be established.

1.3 Imaging irreversibly damaged tissue with MRI

The ischemic penumbra consists of ischemic but viable tissue that may be salvaged through revasculatory treatment such as pharmacological thrombolysis or mechanical thrombectomy. It is, however, due to the risk of unwarranted hemorrhagic or other complications, not appropriate to perform a revasculatory intervention on every AIS patient or in every patient where CCH is suspected. The presence of extensive tissue damage and a low likelihood of remaining penumbra is contra indicative to revasculatory intervention. Identifying irreversible tissue damage in relation to salvageable tissue through imaging is thereby an important aim in the diagnostic process. This is especially relevant in cases of so-called malignant infarction(*27*), where collateral blood flow is hindered by a proximal occlusion in combination with insufficient LMA collaterals. The loss of collateral blood flow will result in fast progression of ischemic injury at the expense of penumbra tissue. In such cases, the potential gain of interventional treatment is outweighed by the high risk of serious adverse events such as hemorrhage. In routine imaging, the two MRI techniques used to identify irreversibly damaged tissue are DWI and T2WI. The vasogenic edema that causes T2 – signal increase is likely caused by blood-brain-barrier breakdown that arises from progressive vasogenic edema. (*5, 28, 29*). T2WI is capable of identifying ischemic injury in the brain, however, it is not adequately sensitive to perform this task in the hyperacute phase of AIS.

1.3.1 Diffusion weighted imaging

On a cellular level, unless blood flow is restored, energy-dependent ion-transporters will fail, causing cytotoxic edema which results in the gradual swelling and ultimately destruction of affected tissues. On a macroscopic level these processes entail a significant reduction of the extra-cellular space which decreases the free diffusion of water molecules.

The application of diffusion weighted imaging (DWI) for the detection of ischemic injury in the brain was introduced in 1990. It first described the rapid and dramatic decline of the apparent diffusion coefficient (ADC) of affected brain regions in cats subject to MCA occlusion(*30*) (for DWI review see(*31*)). Significantly, these changes were detectable before any T2-signal increase. (*5, 28, 29*). To date, DWI

has proven more effective than any other imaging technique, including routinely used CT, for the early detection of ischemia-induced brain damage(*32*).

The methodology of DWI utilizes a pair of opposing diffusion gradient pulses superimposed on a T2-weighted spin-echo pulse sequence. In short, an initial diffusion gradient pulse will assign a spatially specific phase shift to the protons of water molecules contained within an examined area. The subsequent diffusion gradient pulse inverses the previously applied phase-shift, resulting in the complete restoration of phase for stationary protons while moving protons acquire phase dispersal, and thereby signal loss, in proportion to their degree of diffusion. Since DWI is superimposed on a T2-image, it is affected also by the factors contributing to T2-signal, a MRI phenomenon referred to as "T2-shine through". As mentioned previously, T2WI is sensitive to the vasogenic edema that results from ischemic blood brain barrier breakdown. To counteract these confounders, tissue ADC is calculated. In contrast to DWI, an ADC map provides a purely parametric readout of the movement of water molecules in the examined tissue region(*31*).

1.4 Imaging the penumbra

Various imaging methods have been developed to enable the identification of the ischemic penumbra, ranging in their degree of accuracy from those attempting to determine tissue status absolutely, as with Oxygen-15 (^{15}O) based PET tracers, to surrogate readouts such as hypoxia tracers ^{18}F-Fluoromisonidazol ([^{18}F]FMISO) and ^{11}C-Flumazenil ([^{11}C]-FMZ), and non-invasive DWI, perfusion weighred imaging (PWI) and BOLD MRI. The motivation behind seminal attempts to image the penumbra specifically were based on early methods, developed in the 1940s and 50s, in which nitrous oxide or xenon-133 were employed to track regional blood flow dynamics in the context of functional activation of the brain. These methods subsequently became established for studies on AIS(*33, 34*).

1.4.1 Oxygen-15 PET provides gold standard

^{15}O based PET, pioneered in the 1970s, has been extensively used to identify and investigate the metabolic impairments of the ischemic penumbra, and has provided major insights into the pathophysiology of AIS in animal models as well as in humans ((*35-38*), see (*14*)for review). Experimental studies on cats and non-human primates were able to establish that the recruitment of the penumbra to the ischemic core is a gradual process, and provided an in-vivo outline of the emergence of irreversible tissue damage following an acute loss of CPP. These discoveries prompted the understanding of ischemic injury as resulting not only from the severity of the perfusion deficit, but also from the length of time it is in play(*39*). Moreover and significantly, investigations performed in the early 1980s were able to outline the hemodynamic and metabolic detorioration of severly

hypoperfused but viable tissue, the condition described as misery perfusion(*17, 40-43*) and in which a reduction in CBF to 12–22 mL/100 g/min is coupled with metabolic impairment in the form of a ~ 40% elevation of OEF while CMRO2 is sustained more or less at physiological levels. These observations strongly indicated the presence of a time-dependent ischemic penumbra in human stroke patients.

^{15}O is a positron emitting radioisotope with a short half life of 123 s. Several methods for the examination of oxygen metabolism with ^{15}O have been developed. The most established is the steady-state inhalation method pioneered in the early 1980s(*36, 44*). In the steady-state method a continous inhaltion of ^{15}O is utilized. Within approximately 10 min, the kinetics of the radiotracer will have settled into a steady-state between ^{15}O being supplied to the brain through the arterial circulation, the extraction of ^{15}O to brain tissue and the subsequent wash-out of $H_2{}^{15}O$ resulting from cellular respiration. The accuracy of the ^{15}O inhalation method was improved by complementing it with the steady-state measurements of regional CBF. These employ an initial, continous inhalation of ^{15}O-labeled carbon dioxide ($C^{15}O_2$) which is converted to ^{15}O water ($H_2{}^{15}O$) in the lungs and subsequently transported through arterial blood to the organ of interest, such as the brain. If the partition coefficient of water between blood/brain tissue and the $H_2{}^{15}O$ concentration in arterial blood are both known, a calculation of CBF is possible. The ^{15}O inhalation method benefits from the possibility to correct for recirculating $H_2{}^{15}O$ and a mathematical model can be applied to determine regional OEF (*14, 45*). To increase accuracy, the method was refined(*46, 47*) to include also the inhalation of ^{15}O-labeled carbon monoxide ($C^{15}O$) which results in irreversbly radiolabeled red blood cells that can be used to measure CBV.

The impact of ^{15}O PET studies into the progress of AIS during the 1980s and 1990s cannot be overstated, with investigations initialising and augmenting the understanding of the pathophysiological concepts that define the basis for experimental and clinical strategies to date. These studies outlined for the first time the *in vivo* progression of acute cerebrovascular disease. ^{15}O PET was used also to outline hemodynamic and metabolic signatures of CCH; examinations on patiens with chronic carotid occlusion showed extensive regions with decreased CBF, increased OEF but normal levels of CMRO2, consistent with persistent oligemia (*14*). Given that ischemic injury in the brain is a product both of the time and severity of a perfusion deficit, it is to be expected that oligemic tissue may transition into penumbra unless adequate blood flow is restored.The implementation of ^{15}O PET remains the experimental gold standard of penumbra imaging. Nevertheless, due to major logistical drawbacks such as the very short half-life of ^{15}O (123 s) it is highly unlikely that we will we see the routine application of ^{15}O PET in the foreseeable future.

1.4.2 Perfusion Weighted Imaging in ischemic stroke

With the emergence of high-field MRI during the 1990s, perfusion-MRI became a readily available alternative to logistically challenging ^{15}O PET methods. PWI performed with CT or MRI is now a routinely used method for evaluating the severity and spatial distribution of blood flow deficits in AIS. We will focus on PWI obtained by MRI. To date, two methods have been established for the acquisition of PWI with MRI. These are bolus tracking PWI, i.e the first-passage of a highly magnetic intra-venous contrast agent(*48, 49*)], commonly Gadolinium, and arterial spin labelling (ASL). We will focus on ASL-based PWI and two methods used in its acquisition.

Continuous ASL employs magnetic labelling, *tagging*, of arterial blood through the application of an up to seconds long inversion RF pulse to the cervical arteries(*50, 51*). The magnetic inversion of the protons contained in the blood reaching the brain causes a marginal T1-signal loss that is harnessed in a so-called *tag-image,* and which is subsequently compared to a *non-tagged* control. In *Dynamic ASL (DASL)*, the effect of tagged blood on T1-signal is measured at several time points relative to the time of the inversion RF pulse. The benefits of collecting data at several different time points subsequent to labelling is it allows for a better estimation of the biases produced by the T1- relaxation which occurs during the transit time of tagged proton. The transit time, also referred to as inflow time, is the time it takes for the tagged proton to travel from the tagging plane at the location of the cervical arteries to the imaging plane.

Various hemodynamic parameters can be obtained from ASL PWI. Those included in the *central volume principle* (equation 1), in which blood flow is defined as the quotient of blood volume and the transit time of red blood cells through the vascular bed, are the most established.

$$CBF = \frac{CBV}{MTT} \tag{1}$$

Since its emergence, PWI has been proposed as a potential method for the identification of the ischemic penumbra. The specificity of PWI has however remained inconsistent, with a general consensus regarding the correct interpretation of results still lacking. In part, this is caused by the continuous debate regarding the absolute blood flow thresholds separating the penumbra from irreversibly damaged tissue, as well as from so-called oligemic tissue which is not at an immediate risk of infarction(*52*). In a systemic review performed by Bandera et al.(*52*), it was observed that mean values for relevant blood flow thresholds are largely

consistent with those in experimental studies, however, results deviated to such a degree that further validation was deemed required to increase the diagnostic value of PWI. Moreover, several technical issues, such as a lack of standardized, methodological protocols and observer unreliability have limited the use of PWI as a stand-alone diagnostic tool for AIS. Due to these issues, the implementation of PWI has largely been as a component of composite imaging regimes, in particular the DWI/PWI mismatch surrogate of the ischemic penumbra(*2*).

1.4.3 DWI/PWI mismatch as a surrogate of the penumbra

The current consensus regarding the progression of AIS describes the time-dependent and continuous expansion of irreversible damage into regions of ischemic penumbra(*53, 54*). The restoration of blood flow to the hypoperfused areas surrounding the ischemic core, the DWI/PWI mismatch, initially proposed in the mid- 1990s(*2, 55*), has been proposed as a surrogate measure of the penumbra. Although we will focus of DWI/PWI as measured with MRI, a corresponding measurement is available using CT where a perfusion image is compared to a non-contrast image of the ischemic lesion. Lesion expansion occurs predominantly in patients with large mismatches in the early phase of AIS and is present in around 70% of patients(*32, 56, 57*). The DWI/PWI mismatch as a surrogate of the ischemic penumbra is underpinned by observations that the restoration of blood flow inhibits DWI lesion expansion, and by the rapid resolution of neurological deficits found following reperfusion in patients with large mismatch regions(*58, 59*). Over the last decade, DWI/PWI mismatch has been successfully implemented to define the ischemic penumbra in several clinical studies(*8, 60-63*).

An important question of specificity has been directed at the DWI/PWI mismatch as a surrogate marker of the penumbra. Firstly, there is a currently, as pertaining to PWI, a lack of methodological uniformity between centers. This issue is accentuated by the fact that the estimated size of the penumbra varies according to which perfusion parameter is used. Secondly, as mentioned previously, the formation of ischemic injury in tissue results not from the degree of perfusion impairment alone, but rather from the severity as well as the *duration* of a perfusion deficit. This means that PWI does not provide a direct measurement of tissue status, and there is a risk of overestimating the amount of penumbra contained in the DWI/PWI mismatch(*64*). Regardless of the lack of a general consensus on how to best perform and interpret combined DWI and PWI examinations, there are strong arguments for the clinical relevance of DWI lesion expansion at the expense of surrounding hypoperfused regions. Several studies have observed highly variable degrees of ischemic lesion growth in AIS, with slower growth linked to a higher potential to form a significant penumbra and an improved clinical outcome following acute intervention and reperfusion (*65-67*).

1.4.4 BOLD MRI

BOLD MRI(*68*) can be used to examine the metabolic impairment of tissue and has been proposed as an alternative to ^{15}O PET and DWI/PWI mismatch for the identification of penumbra (21). The BOLD methodologies applied in experimental stroke research are various, and largely defined by the capabilities of different centres to obtain readouts of hemodynamic parameters.

The basis for BOLD methodology is the difference in magnetic susceptibility of oxygenated and deoxygenated (dHb) hemoglobin, which are respectively weakly diamagnetic and strongly paramagnetic(*68*). Magnetic susceptibility is a dimensionless property which describes the degree of magnetization of tissue when exposed to a magnetic field. In AIS and CCH, the OEF of the penumbra becomes elevated(*69*). OEF elevation increases the fraction of dHb in the venous blood that is drained from affected tissues. The accumulation of dHb creates mesoscopic magnetic field inhomogeneities which increase the transverse relaxation rates R2 (1/T2) and R2* (1/T2*) of examined tissues. A change in tissue OEF is therefore detectable by employing an MRI sequence sensitive to transverse relaxation, such as gradient echo T2*. If both R2 and R2* are known, the effect of microscopic tissue decay, contained in R2, can be subtracted from R2* to produce R2′ according to equation 2. R2′ more exclusively measures the effect of the concentration of dHb in venous blood and is, considering that R2 has been removed, not as affected by manifest pathology such as vasogenic edema or inflammatory gliosis(*70, 71*). Please see Figure 2 for characteristic examples of R2, R2* and R2′ in an animal subject to M2CAO.

$$R2^* = R2 + R2' \tag{2}$$

1.4.5 Determining Oxygen Metabolism with Quantitative BOLD

The quantitative BOLD (qBOLD) approach was initially developed in the 2000s(*72*). A commonly accepted model developed by Yablonskiy & Haacke defines the relationship between $R2''$ relaxation time, venous dHb fraction and venous blood volume (CBVv) in a network of randomly oriented cylinders(*73*). As a rule, qBOLD regimes now apply T2* gradient echo (GE) as well as T2-weighted spin echo (SE) sequences as readouts of magnetic susceptibility, with the susceptibiliy of the examined tissue proportional to the concentration of dHb. However measuring tissue susceptibiliy with T2* and T2 is not enough to reliably estimate OEF or CMRO2, considering that transverse relaxation is affected also by tissue CBV, CBF, Hct, as well as other contributing factors (*74*). In order to calculate the regional OEF, it is thereofore necessary to differentiate the susceptibility contribution made by

dHb located in the venous compartment from that of dHb contained in the arterial compartment. While the latter is easy to assess by combining a non-invasive pulsoximetry with a Hct blood test, calculation of the dHb concentraion of the venous compartment is more cumbersome and requires a measurement of CBV, which is acquired either by ASL or by the use of highly magnetic contrast agent such as iron-oxide particles. A partition coeffecicient constant can then be factored in to approximate the proportion of CBVv from total CBV. Once an approximate value of CBVv has been determined, OEF can be calculated according to equation (3):

(3)

$$OEF = R'_2 \frac{1}{CBV_v \frac{4\pi}{3} \Delta\chi_0 \, Hct \, B_0 \, \gamma}$$

In this model (2), $\Delta\chi_0$ describes the susceptibility difference between fully oxygenated and fully deoxygenated blood = 0.264 ppm[35], Hct is hematocrit blood fraction, B_0 is magnetic field strength and γ is the gyromagnetic ratio for the proton nucleus = 2.68 x 10^8. The oxygenation fraction of arterial blood is assumed to be 100%, i.e 1/1 (*74-76*). Provided CBF is also known, once tissue OEF has been determined it can be used to calculate $CMRO_2$ according to equation 4(*75*),

(4)

$$CMRO_2 = C_{rbc} \, CBF \, rOEF \, Ya \, Hct$$

in which C_{rbc} is the oxygen carrying capacity of red blood cells (C_{RBC} = 0.493 ml O_2/ ml RBC), *Ya* is the oxygenation fraction of arterial blood and CBF is measured in ml/ 100 g/ min.

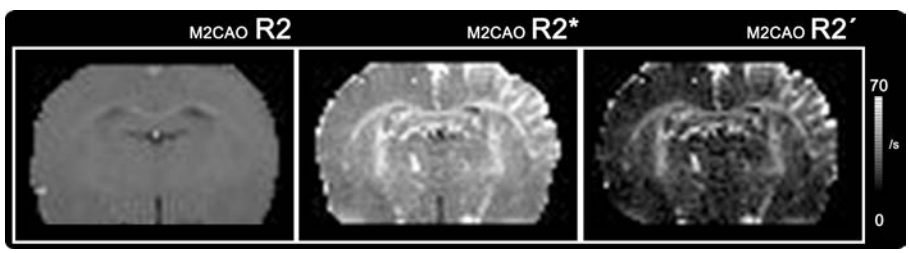

Figure 2. R2, R2* and R2′ images from a single animal. The images are from an examination performed during M2-segment occlusion of the middle cerebral artery (M2CAO). Images are from the same location in the brain. The animal was included in paper III.

1.4.6 Quantitative BOLD in acute ischemic stroke

qBOLD MRI has the capacity to detect metabolic impairments in AIS, thereby identifying tissue-at-risk. Several studies have implemented the qBOLD approach in animals and humans (*75-79*). In a study from 2014(*78*), Christen et al. observed a correlation between areas of decreased oxygen levels as defined by MRI and ex-vivo examination with hypoxia specific biomarkers. Other studies using MRI sequences sensitive to transverse relaxtion have demonstrated how perfusion deficits correlate to increased OEF in AIS patients(*77, 80*). Although highly promising, the qBOLD technique also has challenges such as the need for several examinations and longer examination times than what is necessary with CT.

1.5 Cellular hypoxia in ischemic stroke

Hypoxia occurs when the amount of oxygen supplied to cells becomes inadequate to sustain normal physiological functions. AIS causes ischemia which in turn will result in hypoxia in affected cell populations. In worst case scenarios, hypoxia may result in the cessation of cellular ATP production, leading to an accumulation of cytotoxic edema and ultimately necrosis(*81*). Considering the potential of a single examination capable of identifying the penumbra there have been several attempts to develop radiotracers with the capacity to assess tissue hypoxia in ischemic regions.

1.5.1 PET imaging with tracers for hypoxia

Radiotracers for hypoxia are especially desirable given that no workable method for measuring tissue oxygenation exists in clinical settings. While ^{15}O-PET provides a gold standard for the imaging of oxygen metabolism (see above), the method is invasive and unpractical given the short half-life of ^{15}O (123 s). Other methods exist but are conditioned by their own limitations. BOLD MRI requires a combination of several different examinations. The polargraphic electrode technique is capable of electrochemical detection of oxygen concentrations but is highly invasive and limited to superficial structures(*82*). Near infrared spectroscopy is also limited to superficial structures(*83*).

The 1990s saw the emergence of hypoxia specific radiotracers that benefited from not requiring the arterial blood testing necessary for steady-state ^{15}O imaging. Out of these, the central benzodiazepine receptor ligand [^{11}C]FMZ and the nitroimidazole derivative [^{18}F]FMISO(*84*) have been established in animal studies and used in studies on human stroke patients.

1.3.1.1 [11C]-FMZ

[^{11}C]FMZ binds to the exclusively neuronal and ischemia-sensitive $GABA_A$ receptor which is abundant in the cerebral cortex. Early observations found decreased [^{11}C]FMZ activity in regions of neuronal death following temporary ischemia in baboons(*85*). Experiments on cats subject to MCA occlusion provided encouraging results with regions displaying defects in [^{11}C]FMZ binding closely related to areas with severely depressed oxygen metabolism(*86*). These results were later reproduced in human ischemic stroke patients, with the absence of [^{11}C]FMZ binding found to occur in areas of severe $CMRO_2$ decline(*87*). A subsequent clinical study, investigating the effects of interventional therapy of AIS, reported that hypoperfused tissue could stand to benefit from reperfusion only as long as [^{11}C]FMZ binding was reduced no more than 3.4 times the normal uptake(*88*). The experimental use of [^{11}C]FMZ has in recent years mainly focused on the monitoring continued neuronal loss in the subacute and chronic phase of AIS(*89, 90*).

[^{18}F]FMISO and [^{64}Cu]CuATSM

[^{18}F]FMISO diffuses freely across cell membranes and subsequently undergoes single-electron reduction, transforming into a potentially reactive species. In viable cells with physiological levels of oxygen pressure, it will momentarily be re-oxidized before diffusing back into the extracellular space. During cellular hypoxia re-oxidization is prohibited which results in [^{18}F]FMISO undergoing additional reduction and binding irreversibly to the intracellular compartment (91). Early studies found [^{18}F]FMISO activity surrounding infarcted regions in AIS patients during the first 48 h after ictus. The areas of high [^{18}F]FMISO accumulation were interpreted as representing the ischemic penumbra, motivated by the fact that [^{18}F]FMISO does not access cells that have undergone infarction regions of increased [^{18}F]FMISO uptake did not reappear in follow-up examinations performed between days 6-11(*92*), indicating that the tissue had either perished or resolved back into metabolic homeostasis. [^{18}F]FMISO has since been employed to illustrate how irreversible damage spreads from the center to the periphery of regions suffering ischemia in stroke patients (*93*). Similar results have been found in animal stroke models (*94, 95*). The [^{18}F]FMISO-similar nitroimidazole tracer [^{18}F]FRP170 has been used to reveal hypoxia in regions of increased OEF in cases of CCH(*96*). It is now understood that [^{18}F]FMISO activity in ischemic tissue declines over time(*97*). Nevertheless, question marks remain over the specificity of [^{18}F]FMISO for tissue-at-risk. A validation attempt performed in a limited number of AIS patients observed that [^{18}F]FMISO activity did indeed spike as perfusion declined to levels consistent with those seen in penumbra. However, increased tracer activity was found also to overlap with irreversibly damaged tissue as identified by DWI and with non-symptomatic tissue without any perfusion deficit (*98*). Moreover, a major drawback of [^{18}F]FMISO is the necessity of lengthy examinations due to

the substantial time required for adequate accumulation in hypoxic cells (> 2 h). This makes the clinical application of [^{18}F]FMISO appropriate in cases of CCH and in the subacute rather than the acute phase of ischemic stroke.

Cu-diacetyl-bis(N4- methylthiosemicarbazone) ([^{64}Cu]CuATSM)(*99*) is a hypoxia radiotracer that is considerably less explored than [^{18}F]FMISO in the context of AIS. Similarly to [^{18}F]FMISO, it undergoes passive diffusion into the intracellular compartment where it is reduced to Cu(I)-ATSM. It is subsequently reoxidized back to Cu(II)-ATSM, facilitating wash out, as long as the intracellular concentration of oxygen is normal(*99*). If the cell is subject to hypoxia, however, the Cu(I)-ATSM compound remains in the intracellular compartment, where Cu(I) undergoes further reduction as well as subsequent reactions which leaves it irreversibly trapped within the cell(*100, 101*). [^{64}Cu]CuATSM is especially interesting because it requires significantly less accumulation time than [^{18}F]FMISO, potentially allowing its use in the acute phase of AIS (89). The tracer has already been used with promising results in imaging of tumor hypoxia (*102-104*), and also in ischemia-caused myocardial hypoxia(*101, 105*) as well as in AIS(*106*).

1.6. Acute neuroinflammation in ischemic stroke

An acute inflammatory response is a major component of the pathophysiological processes that follow AIS. Neuroinflammation has been implicated in the emergence of secondary injury after stroke, and in the degree of the resulting brain damage(*107-109*). With AIS treatment now capable of achieving significant neurological recovery, understanding inflammatory responses after AIS is important to further optimize the treatment of stroke patients. Acute neuroinflammation has been described as double-edged sword with potentially both beneficial and detrimental effects on clinical outcome (*110-112*). Long-term consequences of the inflammatory response seem to differ depending on the underlying pathology that causes it. In the context of AIS the acute neuroinflammatory response is typically characterized by early the activation of resident microglia and by the large-scale infiltration by blood-borne macrophages. It is also made up by the recruitment and activation of blood-borne leukocytes, specifically neutrophils and monocytes, and of the morphological changes in astrocytes.

Microglia are the resident phagocytes of the central nervous system and constitute as much as 10% of the total cell population of the brain. In physiological conditions, they maintain a ramified, resting phenotype highly dissimilar to that of the blood-borne macrophage; cerebral insult, however, will initiate a rapid structural remodeling resulting in the amoeboid morphology of the phagocytic microglia (*113, 114*). In tandem with microglia activation, the astrocyte cell population will initiate reactive gliosis in response to ischemic injury. Reactive gliosis permits

the formation of glial scar tissue throughout the rim of injured brain regions(*115*). Although the clinical significance of neuroinflammation in AIS is not yet fully understood, what is clear is that it is a major pathophysiological component during the acute to subacute phases of AIS. Neuroinflammation has been implicated in the emergence and severity of secondary brain injury(113). It may have negative consequences comparable to those attributed to the inflammation and subsequent tissue remodeling that follows myocardial infarction(116).

1.6.1 Profiling neuroinflammation with immunohistochemistry

Histological immunohistochemistry (IHC) analysis is the gold standard for examining neuroinflammatory processes. In microglia and astrocytes, the process of reactive gliosis entails the upregulation of several biomarkers that are readily employed for IHC; the activated microglia increases the amount of complement type 3 receptor Cd11b, which binds to the monoclonal antibody (MAB) Ox42(*113*). The debridement of necrotic material performed by mononuclear phagocytic cells results in the formation of phagolysosomes that are recognized by the MAB ED1(*117*). Anti-glial fibrillary acidic protein (GFAP) is used to examine the activity of astrocytes. However, microglia and monocytes differentiate from the same mesodermal/mesenchymal progenitor, with microglia immigrating to and seeded within the mammal brain during early fetal development(*118*). This entails an all but absent distinction in the surface marker profile between macrophages and the activated microglia phenotype(*119*), and poses a challenge for any attempt to distinguish between the cell types with IHC or PET imaging.

1.6.2 Imaging neuroinflammation with PET

Neuroimaging is capable of examining the inflammatory response that occurs in the subacute and chronic phases of ischemic stroke. When compared to ex-vivo analysis of neuroinflammatory processes, it has the obvious advantage of allowing in-vivo examinations and thereby longitudinal study designs. There are specialized techniques for the identification of inflammatory cells with PET in the form of translocator protein 18 kDa (TSPO) specific radiotracers. The expression of TSPO, previously known as the peripheral benzodiazepine receptor (PBR), is upregulated in microglia and astrocytes in conjunction with reactive gliosis. TSPO upregulation within microglia and monocytes was initially observed inside ischemic lesions by Myers et al.(*120*), and was subsequently documented also in the peri-infarct regions(*71, 121*). TSPO upregulation has since been found also in astrocytes present along the peri-infarct rim (*122*). The substantial upregulation of TSPO in these cell types following various cerebral pathologies has been harnessed in PET employing radioligands against TSPO as a routine technique for imaging of acute neuroinflammation in experimental settings. Several TSPO-

radioligands have been developed for this purpose, with [^{11}C]PK11195 the most established and most commonly used. The various inherent drawbacks of [^{11}C]PK11195, including poor signal-to-noise ratio and the high degree of non-specific binding(*123*), have prompted the development of so-called second-generation TSPO radioligands such as [^{18}F]FEPPA, [^{11}C]DPA-714 and [^{11}C]PBR28. Among these [^{11}C]PBR28 has improved on the disadvantages of [^{11}C]PK11195 and has been employed in several pre-clinical studies including small animal models of experimental cerebral ischemia(*71, 124*).

1.7 Animal ischemic stroke models

Experimental research performed in animal models has been crucial to our current understanding of AIS pathophysiology. The conventional middle cerebral artery (MCA) suture occlusion model (MCAO)(*125*) has become the reliable workhorse of experimental AIS research. However, rather than simulating AIS cases suitable for revasculatory treatment, the MCAO model mimics the severe perfusion impairment and inhibition of collateral blood that occurs in cases of malignant MCA infarction(*27*). Malignant MCA infarction is characterized by extensive regions of irreversible damage that rapidly expand at the expense of penumbra tissue. As in malignant MCA infarction, the irreversible damage caused by the MCAO model is extensive and carries a high likelihood of hemorrhagic complications.

The MCAO model is performed by inserting a suture into the internal carotid artery through a transection of the external carotid artery (ECA). Although the MCAO model has been modified since first described, fundamental problems remain, and a significant contribution to the extensive infarcts seen in the MCAO model is the inhibition of collateral flow through the network of LMAs that connect the supply regions of the major arteries of the brain. In the MCAO model, a filament fills out the lumen of the anterior cerebral artery (ACA), where the tip of the filament is positioned. This results not only in the inhibition of flow through the MCA, but also in a severe reduction of collateral blood flow through virtually all LMAs since the filament obstructs flow both in the ACA and posterior communicating artery (Pcom). While in humans the Pcom is slender, in the rat, the Pcom is a major vessel, arising from the internal carotid artery, and forming an anastomosis with the smaller posterior cerebral artery (PCA) that originates from the basilar artery (*126*). In rats, the Pcom appears to continue beyond its junction with the PCA, providing a direct vascular channel between the internal carotid artery and the caudal regions of the cerebral hemisphere. Branches from the Pcom supply subcortical structures such as the hypothalamus. Distal to the junction of the PCA and the Pcom, the resulting vessel in the majority of animals ramifies into branches supplying the hippocampus and caudal regions of the midbrain, as well as providing leptomeningeal anastomoses with collateral blood flow(*127*). (*127*).

The MCAO model consequently mimics a terminal carotid T occlusion (*125, 128*) with the severe disruption of collateral blood flow typical of malignant infarctions (*129*). Another significant disadvantage of the MCAO model results from the ECA transection used to introduce the suture to the cerebral vasculature. This procedure produces ischemic injury to muscles used for mastication and swallowing, inevitably causing weight loss and suffering in the animal. Furthermore, the ischemic injuries caused to the hypothalamus are prone to produce hyperthermia and disturbance in water homeostasis which are not phenomenons associated with human AIS(*125*).

1.7.1 Middle cerebral artery M2-segment occlusion model in rat (M2CAO)

The papers included in this thesis use the M2-segment occlusion ischemic stroke model in rat (M2CAO). The M2CAO model was developed by Arnberg et al. to improve the translational value of animal AIS research(*130*) and has several advantages to the conventional MCAO model. In short, M2CAO is an endovascular method, performed by guiding a small microwire into the M2 – segment of the MCA under guidance of fluoroscopy imaging. In contrast to the conventional MCAO, the M2CAO model causes only a marginal CBF reduction in the PCA supply region, and does not reduce the perfusion of the ACA supply region to an extent causing ischemic injury, making it more similar to the majority of clinical strokes (carotid T-occlusion and malignant infarction being exceptions). The M2CAO model effectively simulates human AIS cases suitable for intervention, in that the initial volume of irreversible damage within brain regions subjected to M2CAO is limited and surrounded by large regions of potentially salvageable tissue-at-risk(*70*).

The M2CAO model also has the advantage of minimally invasive retraction of the microwire from the M2-segment of the MCA, which achieves reperfusion. Reperfusion can be performed without manipulating the body of the examined animal. This is beneficial when performing imaging studies because examinations can be performed both during M2CAO and after reperfusion without the need to remove the animal from the scanner. Also, in stark contrast to the suture MCAO model, animals subjected to M2CAO are not subjected to the suffering caused by ischemic injuries to muscles involved in mastication and swallowing, or to the detrimental effects of hyperthermia in addition to near hemispheric ischemic injuries(*130*).

2. AIMS OF THE THESIS

The aim of the thesis was to investigate tissue pathophysiology in AIS as modelled by M2CAO, and to use these findings to develop and improve methods for the identification of the ischemic penumbra through imaging with MRI and PET.

The specific aims of each paper were:

(I) To investigate the neuroinflammatory response in the acute and subacute phases of transient M2CAO with the radiotracer [^{11}C]PBR28, and to validate [^{11}C]PBR28 against the gold standard of ex-vivo IHC analysis.

(II) To profile the emergence and expansion of irreversible injury at the expense of ischemic penumbra as defined by DWI/PWI mismatch MRI during M2CAO.

(III) To assemble a MRI protocol capable of investigating the oxygen metabolism of ischemic tissue, and to use this protocol to identify the ischemic penumbra during M2CAO. Then, to compare the MRI protocol with the DWI/PWI mismatch protocol used in paper II.

(IV) To compare the effectivity of PET tracers [^{18}F]FMISO and [^{64}Cu]CuATSM in identifying tissue hypoxia resulting from M2CAO. Subsequently, to investigate the effects of hypoxia in ischemic tissue using ex-vivo IHC analysis.

3. METHODOLOGICAL CONSIDERATIONS

This thesis is the result of data produced using several methodological modalities. These include fluoroscopy (papers I-IV), MRI (I-IV), PET (I, IV) and IHC (I, IV). Detailed descriptions of methodological procedures concerning acquisition and processing of data are available in the original manuscripts. This section, while containing summary descriptions, focuses instead on particular considerations behind the choice of methods.

3.1 Study designs and analysis

3.1.1 Paper I

26 animals were included in the study. Animals were subjected to 90 min M2CAO. Out of these, six animals underwent longitudinal PET examinations with the TSPO targeting radiotracer [^{11}C]PBR28. These examinations were performed in order to profile the emergence and progression of acute neuroinflammation following AIS. Animals were examined with MRI in proximity to PET scans. Examinations were performed on day 1, day 4, day 7 and day 14 after 90 min M2CAO. All 26 animals were included in ex-vivo IHC analysis in order to validate the results of the [^{11}C]PBR28 examinations and to expand the profiling of the neuroinflammatory response. Specifically, the IHC analysis quantified the presence of monocytes/microglia exhibiting TSPO upregulation in and around the ischemic lesion. The analysis also profiled the formation of glial scar tissue by activated astrocytes exhibiting TSPO upregulation in the tissue immediately surrounding ischemic lesions. A separate ICH analysis profiled the progression of debridement performed by phagocytic such as macrophages and activated microglia in ischemic lesions.

Antibodies used for IHC were Cd11b for monocytes/microglia (ab33827, Abcam, Cambridge, UK); GFAP for astrocytes (MAB3402, Cell Signaling Technology, Danvers, MA, US); Cd68 for phagocytic cells (Ed-1, MAB1435, Millipore), NeuN for neuron nuclei (ABN78, Millipore, Bedford, MA) and EPR5384 for TSPO (ab109497, Abcam, Cambridge, UK).

Analysis

The activity of [^{11}C]PBR28 was measured in ischemic lesion regions of interest (ROIs) outlined on T2 images acquired on day 1 after M2CAO. [^{11}C]PBR28 activity in these regions was quantified as standardized uptake values (%SUV) which were normalized for injected dose and animal weight and were compared to contra lateral control regions. PET data was analyzed in (PMOD Technologies Ltd., Zurich version: 3.3). Student´s two tailed paired t-test was used to test for statistical significance.

The IHC analysis consisted of two separate data sets. In the first data set, the ischemic lesion ROI was defined as regions largely devoid of viable GFAP+ astrocytes. Cd11+ and GFAP+ cells, with or without TSPO co-localization, were counted on either side of the glial rim surrounding the ischemic lesion (Metaviewer software, Metasystems). In the second set, Cd68+ cells were quantified within ischemic lesions. The borders of the ischemic lesion were outlined by the presence of neurons exhibiting pyknotic morphology consistent with ischemic injury. ImageJ (National Institutes of Health, Maryland, USA) software was used to count cells within the ischemic lesions. One-way ANOVA corrected for multiple comparisons through Tukey post hoc test was used to test for statistical significance in both IHC data sets.

3.1.2 Paper II

25 rats were divided into three groups subjected to Short (90 min), Intermediate (180 min) or Extended (600 min) M2CAO (Figure 3). M2CAO was followed by reperfusion. Animals were examined repeatedly every 30 min with T2, DWI and PWI during M2CAO and reperfusion. Animals belonging to the Extended group also underwent follow-up examinations on the following day. The assembled data was used to profile injury progression in the hyperacute and acute phase of AIS as modelled by M2CAO.

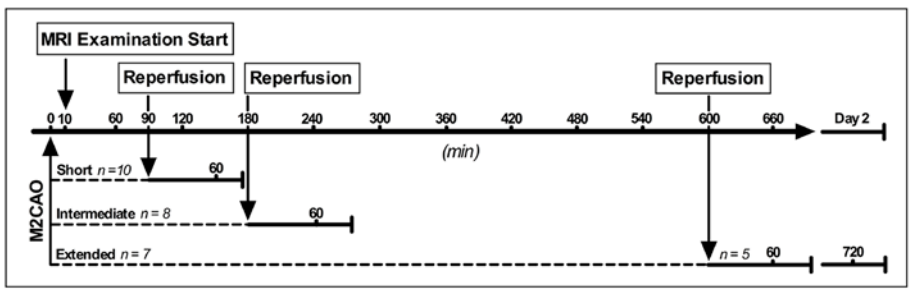

Figure 3. Study design of paper II.

Analysis;

ImageJ and ITK-SNAP software were used for ROI segmentation(*131*). Please see Figure 4 for visual descriptions of ROIs. In order to profile the severity of ischemic injury, the progression of ADC decline and T2WI signal increase, as well as lesion volume progression, was measured across the repeated examinations performed in each animal. The data was fitted to a mixed effects statistical model which is a standard method for the analysis of repeated measurements data and uses the modelling time as a regression variable. This was especially appropriate in view

of our study design. The method allowed us to incorporate all the collected data points, thereby strengthening the quality of the analysis. As well as tracking the severity of ischemic injury, we documented CBF in four regions that will now be described: The ischemic core ROI (IC) consisted of regions exhibiting ADC decline and was delineated in the first examination performed after reperfusion. IC ROIs were subsequently transferred to the CBF map from the first examination after M2CAO in the same animal, and used to delineate the penumbra ROI which matched the DWI/PWI mismatch. Supply regions of the ACA (supero-medial cortex) and the PCA (thalamus, parts of the hypothalamus) were also outlined into individual ROIs. Regional CBF levels were examined for correlations using Spearman coefficients. Longitudinal CBF of the IC and PEN were also compared to control regions in the healthy hemisphere using paired students t-tests.

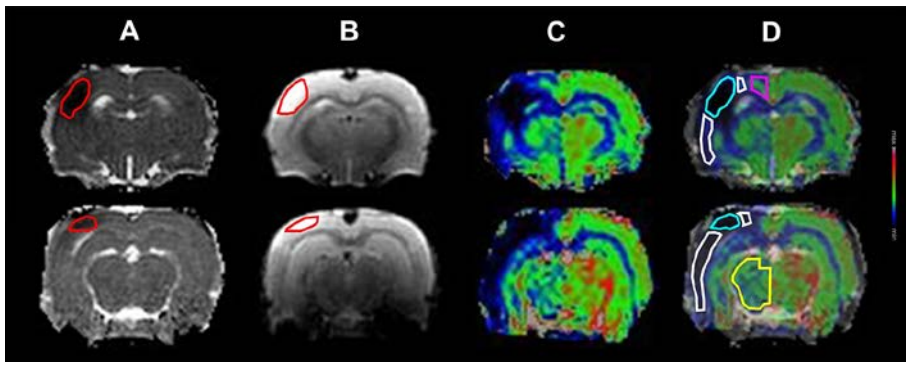

Figure 4. Regions of interest (ROIs) used in paper II. (A) Ischemic core regions (red) seen in apparent diffusion coefficient maps (A) and T2-weighted images (B) (C) Cerebral blood flow (CBF) maps. (D) CBF maps overlain with ADC maps. ROIs used to examine the CBF of the Ischemic Core (cyan), penumbra (white), anterior cerebral artery supply regions (purple), and posterior cerebral artery supply region (yellow).

3.1.3 Paper III

20 animals were included in the study prior to exclusions. Animals were subjected to ~ 80 min M2CAO and were imaged with the imaging protocol shown in Figure 5 during M2CAO and after reperfusion. The protocol included: DWI to outline irreversible damaged, ischemic core regions; multi echo multi slice (MEMS) and Multi gradient echo 3D sequences (MGE3D) to obtain R2 and R2*, respectively; continuous ASL to calculate CBF and; turbo DASL (T-DASL) to determine CBV. Readouts were combined in a qBOLD regimen and used to determine levels of OEF and CMRO2 in the ischemic tissue of animals subjected to M2CAO.

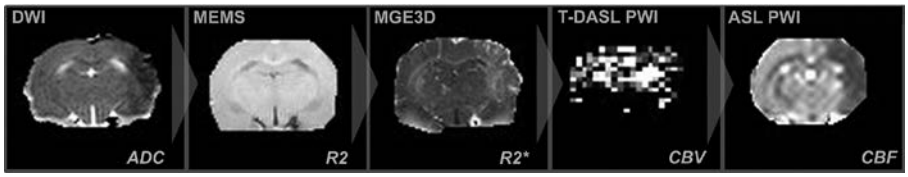

Figure 5. Imaging sequence used in paper III.

Analysis

The ischemic core ROI (IC) was manually traced in ADC-maps and defined as regions with an apparent decrease in ADC. IC ROIs were subsequently transferred to CBF and OEF maps where, respectively, regions of perfusion deficit as well as OEF elevation were outlined in tissue not included in the IC. The volume of the ischemic core- OEF elevation (IC-OEF) mismatch was compared to the volume of ischemic core-CBF perfusion deficit (IC-CBF) mismatch.

We also examined effects of M2CAO and reperfusion on the absolute levels of OEF and $CMRO_2$ in severely ischemic but still viable tissue. These regions were outlined in CBF maps as tissue with normal perfusion but CBF levels of 12–22ml/100 g/min which is consistent with levels attributed to the penumbra (*132*). Healthy contralateral regions were used as controls. Student´s two tailed paired t-test was used to test for statistical significance.

3.1.4 Paper IV

Animals underwent ~ 2 h M2CAO and were subsequently examined with either [^{18}F]FMISO (n=12) or [^{64}Cu]CuATSM (n= 6). Animals were injected with pimonidazole hydrochloride (Hypoxyprobe-1^{TM}, Hypoxyprobe Inc., Burlington, MA, USA) approximately 30 min before the start of M2CAO. The [^{64}Cu]CuATSM group was also examined with DWI MRI to enable an independent confirmation of ischemic lesions. Animals in the [^{18}F]FMISO group were not, however, examined with MRI due to a positive correlate for ischemic injury already achieved by the use of pimonidazole which corresponds to [^{18}F]FMISO uptake. In addition to in-vivo PET, ICH immunofluorescent analysis was performed with antibodies for hypoxia (pimonidazole), neuronal nuclei (NeuN) and astrocytes (GFAP). The objective of the IHC analysis was to determine levels of hypoxia in neurons and astrocytes within ischemic regions. The experimental protocol is illustrated in Figure 6.

Analysis

In the [^{18}F]FMISO group, hypoxic regions of interest were manually outlined around tissue exhibiting an apparent uptake in [^{18}F]FMISO within the cortical hemisphere subjected to M2CAO. A similar analysis was performed in the animals examined with [^{64}Cu]CuATSM, but here ROIs were defined according to ischemic core lesions present in DWI MRI. Control regions were placed in the contralateral cortex.

The PET data was quantified as SUV%. The ICH data was analyzed using an in-house ImageJ script. The script analyzed the intensity levels of pimonidazole within astrocytes and neurons present in hypoxic regions in the cortical regions subjected to M2CAO. Healthy cells located in control regions of the contra lateral hemisphere were used as controls. Student´s two tailed paired t-test were used to test for statistical significance.

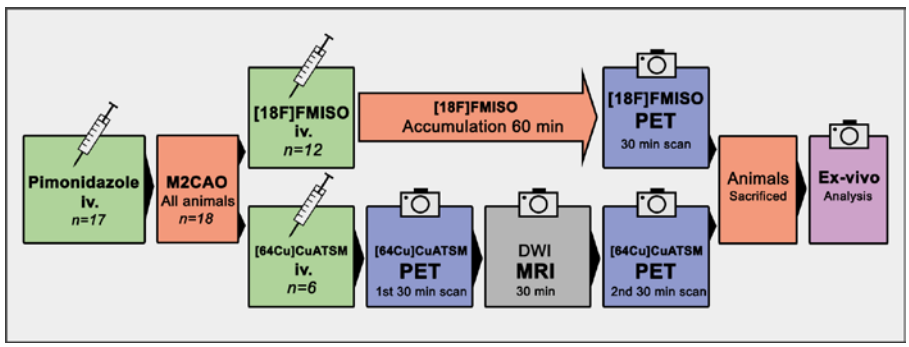

Figure 6. The experimental protocol used in paper IV.

3.2 Animals and ethical considerations (Papers I-IV)

All animal experiments were performed following the guidelines

of the Swedish National Board of Laboratory and the animal welfare board of Karolinska Institutet. Experiments adhered to protocols approves under a protocol approved by the Ethics Review Board of Northern Stockholm, Sweden, and to the ARRIVE guidelines of animal research.

In all, 89 naive, male Sprague-Dawley (SD) rats weighing 300-450 g were used in papers I-IV. Animals were subjected to M2CAO with durations 90 min (paper I-II), 80 min (paper III) and 110 min (paper IV). In paper II, two subgroups of animals were subjected to significantly longer M2CAO durations of 180 min (n=8) or 600 min (n=7). In the longitudinal study design used in paper I, the M2CAO model

caused only a limited amount of suffering for the animal. Animals received general anesthesia with an Isoflurane/air mixture, as well as a local anesthetic at the point of incision in the tail of the animal. Vital signs were monitored throughout surgical procedures and throughout imaging examinations with MRI and PET. Injections of PET radiotracers were performed through a cannula inserted into one of the tail veins. Animals were sacrificed through decapitation while in deep general anesthesia.

3.3 The use of the M2CAO model (Papers I-IV)

Detailed surgical procedures of the M2CAO model have been previously described(*130*). The procedure was performed using X-ray fluoroscopy (Philips Allura Xper XD20 Interventional X-ray system, Philips Medical Systems) (Figure 7.A). A 0.007-inch microwire (Hybrid; Balt Extrusion, Montmorency, France), sheeted inside a 0.020-inch microcatheter (Ultraflow; Covidien, Mansfield, MA, USA), was introduced in the proximal ventral tail artery. The microcatheter was advanced to the proximal descending aorta. The tip of the microwire was subsequently navigated and positioned in the M2 segment of the MCA, causing occlusion (Figure 7.B). The M2CAO model was used for the many benefits described above. Foremost the M2CAO model was designed to increase the translational value of experimental AIS by replicating the pathophysiology and the circulatory impairment present in those AIS patients who are suitable candidates for acute intervention(*130*). These include the he sustained functionality of LMAs which enables the formation of significant regions of hypoperfused yet viable tissue adjacent to the ischemic core, i.e large DWI/PWI mismatch regions.

In paper II, using the M2CAO model enabled us to examine the spread of the ischemic core at the expense of the DWI/PWI mismatch as imaged with MRI. In paper III, we were able to measure the size of regions with increased OEF and compare it with the size of the DWI/PWI mismatch. In paper I, a longitudinal study design was used to examined the neuroinflammatory reaction during the first 14 days after M2CAO. In paper II, follow up examinations were performed on day 1 after M2CAO in a subgroup of animals. It is our opinion that the quality of the results obtained in these studies was possible because of the limited neurological damage incurred by animals subjected to M2CAO, as well as by avoiding the detrimental side effect produced by the MCAO suture model.

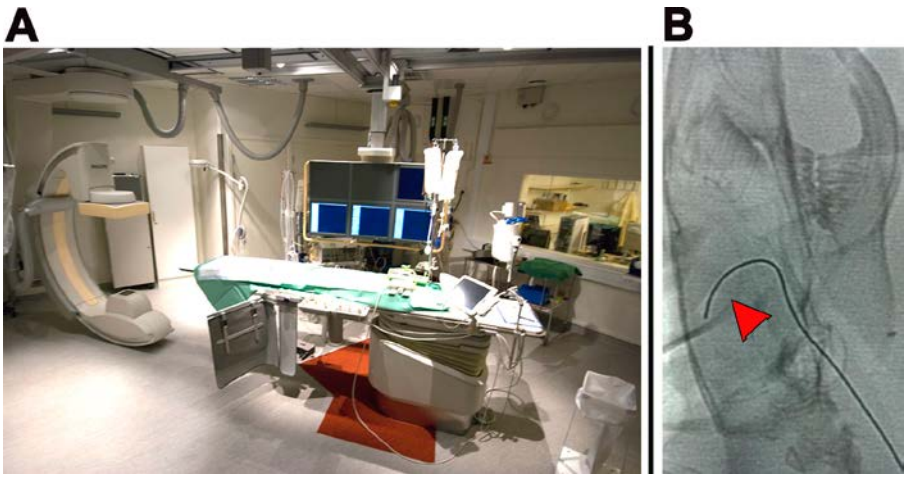

Figure 7. A: The Philips Allura Xper XD20 Interventional X-ray system, Philips Medical Systems, used to perform middle cerebral artery M2-segment occlusion (M2CAO) in rat. B: Fluoroscopy image of the head of a rat (sagittal projection). A guidewire has been placed in the M2 segment causing M2CAO.

3.4 Magnetic resonance imaging (Papers I-IV)

MRI was used in paper I-IV. MRI was used due to its versatility and capacity to produce high resolution images of anatomy (T1), vasogenic edema (T2), cytotoxic edema (DWI), perfusion (PWI), as well as tissue oxygenation (T2*). In papers II-IV, animals were scanned in a 9.4 T magnet (Varian, Yarnton, United Kingdom) during M2CAO and after reperfusion. In paper I, animals were scanned in a Mediso nanoscan PET/MRI (Mediso Medical Imaging Systems Ltd. Budapest, Hungary) on day 1, day 4, day 7 and day 14 after M2CAO. Animal vital signs were monitored throughout MRI examinations.

3.4.1 Imaging irreversible tissue damage – T2WI and DWI (Papers I-IV)

T2WI was used to identify irreversibly damaged tissue through the presence of vasogenic edema which results from blood brain barrier breakdown (papers I, II). DWI was used to identify the cytotoxic edema and thereby the tissue damage which appears very rapidly after M2CAO (papers II-IV). While T2WI is not sensitive enough to detect the emergence of irreversibly damage in the hyperacute phase of AIS, it is well suited for the detection of tissue injury in the subacute to chronic phases. The use of DWI was motivated by the fact that it is the most sensitive method available for the detection of tissue injury in the hyperacute phase *in-vivo*.

DWI was acquired by multi-slice three-shot spin-echo echo-planar imaging. Repetition time (TR): 3 s, echo time (TE): 25 ms, field of view (FOV) of 32 x 32 mm, matrix size of 96 x 96 zero filled to 128 x 128 resulting in an in plane resolution of 256 μ m. Diffusion gradient duration (Δ): 2.3 ms, diffusion gradient separation (δ): 6.5 ms. Diffusion sensitizing gradients were applied along 12 directions with a b value = 1000 s/mm2 and a control image collected twice with the diffusion sensitizing factor b = 0. ADC-maps (mm2 /s) were calculated from the collected data. In paper I, T2WI was acquired through a fast spin echo sequence. In paper II & IV, T2WI was acquired with the same technical specifications listed above for DWI.

MEMS (paper III)

In paper III, T2WI was acquired through a multi-echo-multi slice sequence (MEMS) with 16 evenly spaced echoes with TE 6.94-110.98 ms in order to acquire quantitative T2-maps. The use of MEMS was motivated by the fact that sequences with a single TE would not have allowed us to determine the contribution to signal intensity arising from effects caused by flip angel, proton density, saturation effects from T1, etc. By using MEMS, it was possible to calculate the voxel wise time of T2-decay. MEMS data was processed in the software VnmrJ (Agilent Technologies, Santa Clara, CA, USA). A single exponential decay function was fitted to the magnitude images produced from MEMS data to acquire R2 maps.

3.4.2 Measuring CBF and CBV - Arterial Spin Labeling (Papers II, III)

ASL PWI was chosen rather than contrast enhanced PWI for several reasons. Firstly, ASL is non-invasive and does not require a venous injection of contrast agent. Secondly, in papers II-III, animals were examined repeatedly in proximity, which, due to the necessary wash-out time of contrast agents such as gadolinium, was possible only by the use of ASL(*133*). Finally, ASL allow the quantitative calculation of CBF (paper II-III) according to a well-established model originally described by Silva et al (*134*).

Continuous ASL

Continuous ASL PWI (paper II & III) was acquired by single-shot, gradient echo planar imaging in conjunction with continuous ASL by the application of off-resonance radio frequency power to the ASL coil concurrently with a 1 Gauss/cm gradient during TR. The position in the center of the applied slice package was located 2.4 cm downstream of the labelling plane. As well as tagged images, non-tagged control images were acquired with 25 repetitions per slice. Continuous ASL data was processed into CBF-maps (*134*)

Turbo Dynamic ASL

In paper III we used a technique known as T-DASL to measure CBVa according to a model previously described Meng et al (*51*) (Equation 5). In T-DASL, blood tagging and image acquisition are interleaved which enables a shorter acquisition times at the expense of a somewhat decreased labelling efficiency. The CBVa derived from T-DASL data was used to calculate values for OEF and $CMRO_2$ in paper III. OEF, which was the main focus of results presented in paper III, is proportional to R2' and to CBVv. CBVv was derived from CBVa by the use of an arterial-venous partition fraction of 0.25(*135*). A summary description of T-DASL data acquisition is provided below and illustrated in Figure 8.

The T-DASL acquisition began with a 10 s recovery period in order to establish magnetization equilibrium. An excitation pulse, as well as an echo planar imaging readout module, were subsequently repeated 888 times (TR:67 ms) during the first 60, resulting in 888 images. Blood tagging was applied during the recovery times that occurred between excitation pulses and readout modules in 5 s periods which were repeated 5 times. After each 5 s period, tagging was stopped for 5 s in order to reestablish the steady state and to obtain non-tagged control images. After repeating this cycle 5 times (i.e at the conclusion of the 60 s scanning duration), the whole 60 s cycle was repeated but this time in the presence of vascular supression. Vascular suppression was achieved by utilizing of a pair of 1 ms gradients pulses which were applied parallel and antiparallel to the readout gradient direction. The acquired data was processed according to in-house Matlab (Mathworks, Nantucket) scripts, and the processed data fitted to equation 5 in order to calculate CBVa(*51*).

(5)

$$CBV_a = \frac{\Delta M(0)/M_0(0) - \Delta M(b)/(M_0(b)}{2\alpha_a \cdot \xi - \Delta M(b)/(M_0(b)}$$

In Equation 5, $\Delta M(0)$ and $\Delta M(b)$ define the difference between the first and last signal acquired during each 5 s T-DASL/readout cycle with (b) and without (0) vascular supression. $M_0(0)$ and $M_0(b)$ are the completely relaxed, initial signals acquired during each 5 s T-DASL/readout cycle with (b) and without (0) vascular supression. $2\alpha_a$ is the tagging efficiency achieved at position of the labelling plane. ξ describes the transverse relaxation rates R2* of blood and tissue, and is, due to the short TE used during acquisition, equal to 1.

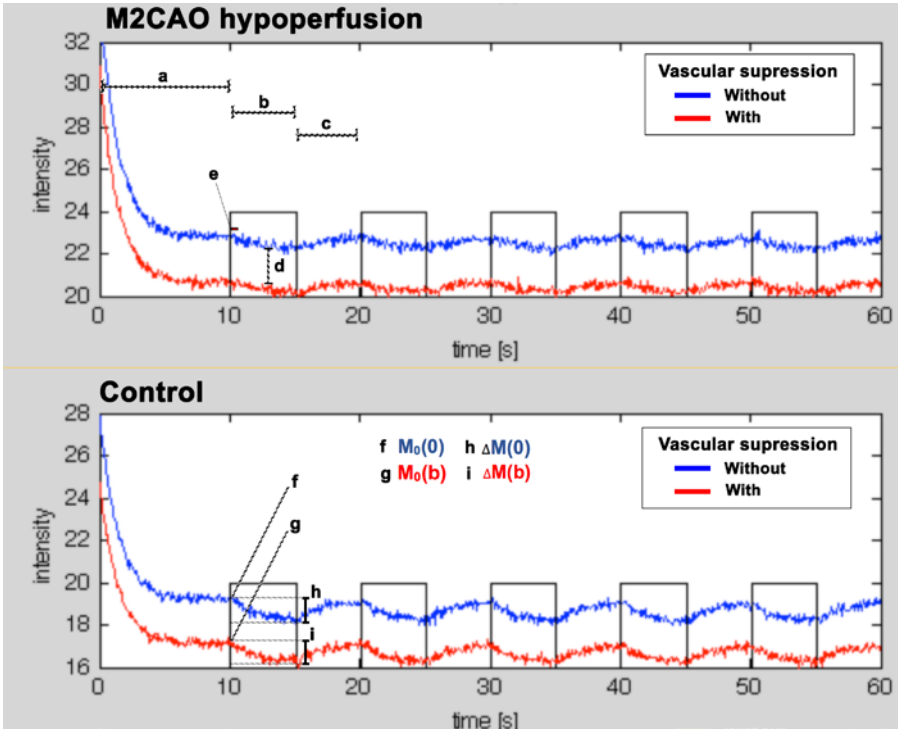

Figure 8. MR signal collected from a region of hypoperfusion resulting from M2CAO (top panel) and from a healthy contra lateral control region (bottom panel). Panels show the 60 s cycle of T-DASL acquisition. Top panel: (a): The initial 10 s during which equilibrium magnetization was allowed to recover. (b): 5 s interleaved excitation/ASL tagging pulse/readout. A clear drop in signal is visible as tagged blood reaches the imaging plane. The drop is less pronounced in the hypoperfused region than in the control region due to the decrease in CBF resulting from M2CAO (c): The 5 s period during which the steady state was reestablished and non-tagged control images were collected. (d): The difference in intensity between images collected with and without vascular supression. The signal difference consists of the vascular signal component. (e): The approximately 1 s inflow time during which tagged blood transits from the labeling plane to the imaging plane. Bottom panel: (f, g): $M_0(0)$ and $M_0(b)$ are the completely relaxed, initial signals acquired during each 5 s T-DASL/readout cycle with (b) and without (0) vascular supression. **(h,i)**: $\Delta M(0)$ and $\Delta M(b)$ and define the difference between the first and last signal acquired during each 5 s T-DASL/readout cycle with (b) and without (0) vascular supression.

3.4.3 Imaging tissue oxygenation with MGE3D T2* (Paper III)

Quantitative T2* imaging was used as the oxygen sensitive readout with which to establish R2′, and subsequently to calculate OEF and $CMRO_{2,}$ in the qBOLD regimen employed in paper III. T2* imaging was acquired with a MGE3D sequence with the following specifications: 12 evenly spaced TE ranging from 2.19 to 37.21

ms, a flip angle of 13 and TR: 70 ms. The acquired data underwent several steps of processing using in-house MATLAB scripts. The end product of the processing was R2* maps corrected for macroscopic field inhomogeneities. The R2* maps were subsequently matched with R2 maps, produced from MEMS imaging, and R2′ was calculated.

3.4.4 Calculation of OEF and CMRO2 maps (Paper III)

OEF and $CMRO_2$ maps were calculated according to equations 2 and 3 using in-house MATLAB scripts. Regularization to 1 was performed in such voxels where the calculated OEF equaled values > 1. Regularization was motivated by the fact that the extraction of oxygen in those voxels where OEF > 1 was deemed to be at its physiological maximum (100%).

3.5 Positron emission tomography (Papers I, IV)

3.5.1 [^{11}C]PBR28 (Paper I)

The [^{11}C]PBR28 radiotracer was chosen due to improved signal-to-noise ratio and a decreased amount of non-specific binding when compared first generation TPSO-probes. Animals were examined on days 1, 4, 7, and 14 after undergoing 90 min M2CAO. The mean injected radioactivity was 17.0 ± 1.0 MBq. Data was reconstructed into 25 time frames. A 3-dimensional penalized maximum likelihood algorithm image reconstruction was performed using 20 iterations (MLEM; TeraTomoTM ; Mediso Ltd.).

3.5.2 [^{18}F]FMISO and [^{64}Cu]CuATSM (Paper IV)

[^{18}F]FMISO was used because it is the most investigated and most established PET radiotracer for the identification of cellular hypoxia resulting from AIS. Although the capacity of [^{18}F]FMISO to identify hypoxia was not in question, the fact that the tracer requires a significant accumulation time before examinations can be performed underpins the interest in finding alternatives which could be applied in the hyperacute phase of AIS. One such alternative is [^{64}Cu]CuATSM. In the [^{18}F]FMISO group, animals were administered [^{18}F]FMISO within 30 min of the start of M2CAO. The average injected [^{18}F]FMISO dose was 38.0 MBq. The radiotracer accumulated for 1 h before PET examinations were initiated. Images were collected every third minute for a total scan time of 30 min. In the [^{64}Cu] CuATSM group, radiotracer was administered 15 min after the start of M2CAO. The average injected dose was 20.4 MBq. Two 30 min PET examinations were performed. The initial examination was commenced right after the administration of [^{64}Cu]CuATSM. Animals were moved to and examined in the MRI scanner at the end of the first PET examination. At the completion of the MRI scan, animals

were returned to the PET scanner where a second examination was begun. The image reconstruction was performed through standard 2D filtered back projection employing ramp filter. The reconstructed images had matrix sizes of 128 x 128 x 95 and a pixel resolutions of 0.9 x 0.9 x 0.8 mm.

3.6 Immunohistochemistry (Papers I, IV)

Brains used for ICH analysis was fresh frozen immediately after being extracted from the animals. The tissue was subsequently sectioned at 12-14 µ. Immunofluorescent IHC was performed using standard protocols that included tyramidine signal amplification (TSA) (*136*). Please see original papers I & IV for detailed protocols. At the conclusion of ICH stainings, sections were scanned with 20x primary objective initial image capture on a Vslide slide scanning microscope (Metasystems, Altlußheim, Germany). Initial captures were stitched in the Vslide software (Metasystems) in order to assemble sectional images with microscopic resolution. In paper I, a data set using the antibodies NeuN and Cd68 was analyzed from micrographs collected through the use of a digital camera (Axiocam MRc5, Carl Zeiss AG) attached to a Zeiss microscope (Carl Zeiss AG, Jena, Germany).

3.6.1 Profiling neuroinflammation

The antibodies used in the IHC analysis in paper I were selected on the basis that they should provide adequate specificity for those cell types exhibiting increased levels of TSPO during the inflammatory reaction that follows AIS. These cell types include activated microglia, the resident immune cells of the CNS, but also monocytes/macrophages, as well as reactive astrocytes involved in glial scar formation and that are detectible with GFAP. Cd11b, was deemed a suitable biomarker considering it is not specific to microglia but is sensitive also to monocytes/macrophages. This allowed us to profile the full range of the neuroinflammatory reaction rather than microglia activation exclusively. The anti-TSPO antibody EPR5384 was used to profile the TSPO expression in these cell populations.

3.6.2 Profiling cellular hypoxia

In paper IV, we used an anti-pimonidazole antibody to correlate the in-vivo uptake of [^{18}F]FMISO to ex-vivo IHC. Pimonidazole comes from the same Misonidazole family of compounds as [^{18}F]FMISO and is a well-established biomarker for hypoxia.

We analyzed the distribution of pimonidazole in tissue and also the levels of pimonidazole exhibited by neurons (NeuN) and astrocytes (GFAP).

4. RESULTS AND DISCUSSION

The following section presents the most significant results contained in each of papers I-IV. Please see the original publications for a complete account of results, as well as for details on animal exclusions.

4.1 Paper I

4.1.1 Early Increase of [^{11}C]PBR28 uptake in ischemic lesions

In paper I we used [^{11}C]PBR28 PET to examine longitudinally the emergence and progression of the neuroinflammatory response after 90 min M2CAO. PET results revealed significantly increased levels of TSPO within ischemic lesions on days 4, 7 and 14 after M2CAO, with the largest increase observed on day 4. No significant increase occurred in the contra lateral hemisphere at any time point. Please see Figure 9.A for an example of [^{11}C]PBR28 PET uptakes on day 1 and 4 after M2CAO.

4.1.2 Immunohistochemistry reveals early monocyte/microglia activation

PET examinations were complemented with immunofluorescent IHC analysis. Results are presented in Figure 10. On day 1, Cd11b positive+ cells of circular appearance were observed throughout lesions. Out of these only a small fraction exhibited TSPO upregulation. These cells were interpreted to be non-TSPO upregulating cells such as neutrophils, which are known to arrive early after a cerebral insult(*109, 113*). The analysis subsequently confirmed PET results by revealing a large increase in activated monocytes/microglia (Cd11b+/TSPO+) cells, as well as an increase in reactive astrocytes (GFAP+/TSPO+), in particular in the periphery of the lesion on day 4. From day 7, a significant increase of reactive astrocytosis in the form of glial scar formation was clearly visible around ischemic lesions. Please see Figure 9.B for confocal microcopy showing the co-localisation of Cd11b/TSPO and GFAP/TSPO.

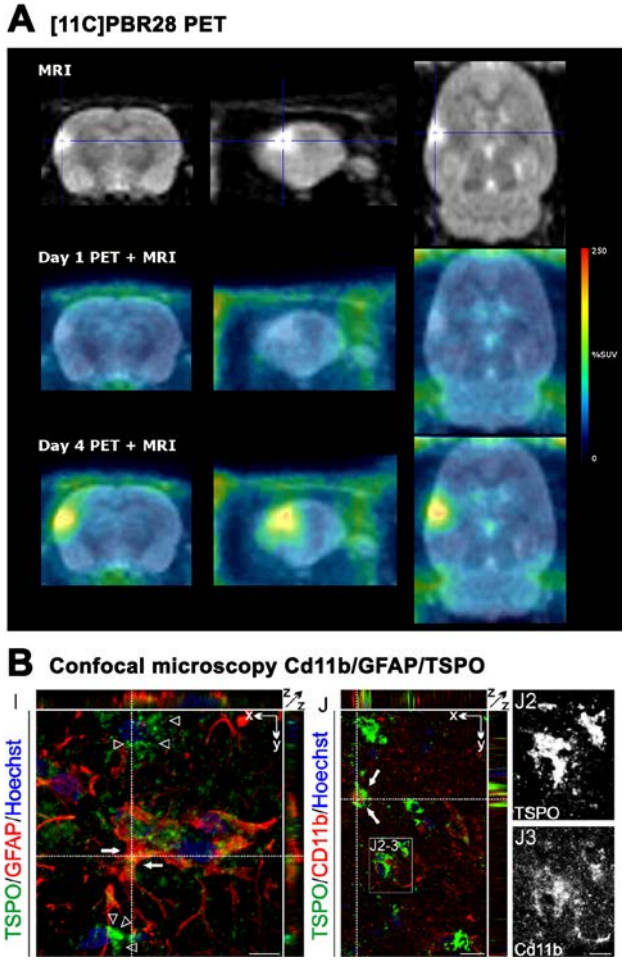

Figure 9: A: Representative %SUV image of [11C]PBR28 uptake from day 1 and day 4 overlaid on the average of all T2 MRI scans taken of the same animal across time points. B: Reconstructed confocal laser scanned micrographs at 4 days after M2CAO. I: GFAP+/ TSPO+ colocalisation in reactive astrocyte (closed arrows). Open arrowheads TSPO expression in cells negative for GFAP. j1–j3 Cd11b+/TSPO+ colocalisation in activated microglia/monocyte (closed arrows).

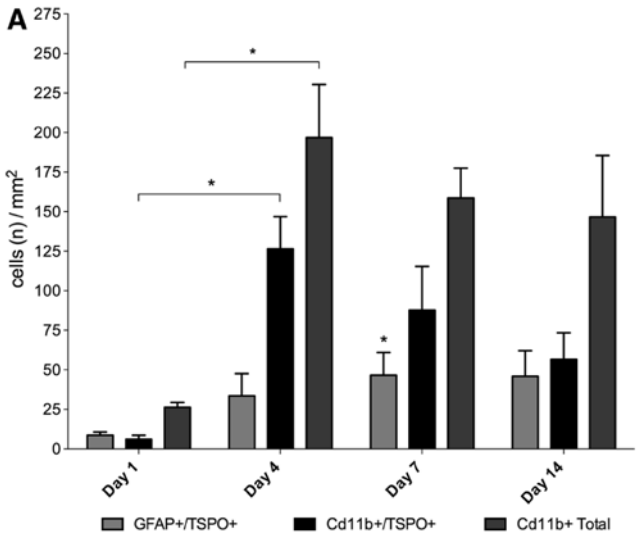

Figure 10. Progression of GFAP+/TSPO+, Cd11b+/ TSPO+ and Cd11b+ (total) cell load in ischemic regions of interest, from day 1 to day 14 after 90 min middle cerebral artery M2-segment occlusion (M2CAO).

The number of Cd11b+/TSPO+ activated monocytes/microglia decreased after day 4, but the total number of Cd11b+ cells continued to increase. On day 14, large and weakly Cd11+ cells exhibiting marginal TSPO intensity were the most common morphological type present in the lesion core. This was interpreted as an increase in the amoeboid, phagocytic phenotype of fully matured phagocytic cells at the expense of the immature/resting phenotypes of monocytes/microglia. However, cells exhibiting high TSPO intensities remained and were predominantly located in and around the newly formed glial scar.

The neuroinflammatory reaction after AIS is a substantial component of the secondary injuries that occur in the days and weeks that follow the ischemic insult (*108, 137*). The activation of microglia will entail a transformation from the ramified morphology, inherent to resting cells, to the large so-called amoeboid type which is hard to differentiate from those macrophages that enter the brain and which perform the debridement of necrotic tissue.

Activation of microglia can be described as a double edge sword; beneficial effects such as the debridement of necrotic tissue and the promotion of large-scale tissue repair are counteracted by the production of proinflammatory mediators linked to a worsening of brain injury through the destruction of the neurovascular unit, as well as contributing to neuronal death by promoting apoptosis(*137*). The possibility to

better monitor and diagnose inflammatory progression is a long-standing objective in experimental as well as clinical AIS research. Experimental studies have now implicated microglia in the loss of BBB integrity(*138*), and demonstrated how up-regulating the M2 anti-inflammatory subtype of microglia at the expense of the proinflammatory M1 subtype benefits neurological outcomes(*139*). Thus far there are no effective therapeutic agents for the treatment of neuroinflammation following AIS, but in the future such agents may be developed. For this reasons an imaging probe capable of accurately examining tissue inflammation in the subacute phase of AIS is of high clinical relevance. [^{11}C]PBR28 is well suited to this purpose.

4.2 Paper II

M2CAO produced a rapid accumulation of focal, cytotoxic edema that could be identified as restricted diffusion in ADC-maps as early as 10-30 min after the start of M2CAO (Figure 11.A). Results showed this rapid phase of increasingly restricted diffusion to occur predominantly during the initial 120-180 min following M2CAO, giving rise to ischemic core regions. There were similarities between the emergence of cytotoxic and vasogenic edema. The T2 signal in the ischemic core increased faster during the initial 120 min following M2CAO only to stabilize in a close to linear progression during subsequent time points (Figure 11.B). Reperfusion produced a trend towards ADC normalization, while the rate of T2 signal elevation increased.

4.2.1 Ischemic core expansion within DWI/PWI mismatch

M2CAO produced a dramatic decrease in the CBF level of the ischemic core. Accordingly, the growth and progressive severity of the ischemic core was rapid in the initial phases. However, the continued expansion of irreversible damage was slow, and did not grow to encompass the entire region of DWI/PWI mismatch, even at 10 h of M2CAO. As in the ischemic core, CBF levels of the DWI/PWI mismatch, i.e. the penumbra ROI, were severely reduced by M2CAO. Results from the regional CBF analysis revealed, however, an incremental increase in the CBF levels both in the IC and the penumbra. We interpreted this as an effect increased collateral blood flow caused by the of the recruitment of LMAs. To confirm the sustained functionality of LMAs during M2CAO, the regional CBF of the penumbra and the ischemic core were correlated to the CBF levels present in the supply regions of the ACA and PCA which are not significantly affected by M2CAO. There was indeed a significantly stronger CBF correlation between the penumbra and the ACA than between the ACA and the ischemic core. The relative difference provides a strong indication of the beneficial effects of LMA recruitment on penumbra survival. Results are in agreement with previous reports describing how the rapid dilation of LMAs following MCAO causes a significant increase in the CBF of ischemic regions(*18, 20*).

The growth rate of the ischemic core in human AIS has been described as highly varying(*65-67*). The Ischemic core expands, as visualized with DWI MRI, in approximately 70% of patients and predominantly in cases where the acute phase DWI/PWI mismatch is large (*32, 56, 57*). Paper II showed a 11 percentage point increase of the ischemic lesion size when normalized against the size of the initial perfusion deficit caused by M2CAO. After 600 min M2CAO, the size of the ischemic lesion was at 27% of the initial size of perfusion deficit. This is comparable to human patients where the DWI/PWI mismatch after 10 h of occlusion has been measured at 30%, although in those cases a further increase in the size of the ischemic lesion was documented in follow up examinations performed several days later(*56*). Please see Figure 12 for an example of how the DWI lesion expands at the expense of the DWI/PWI mismatch.

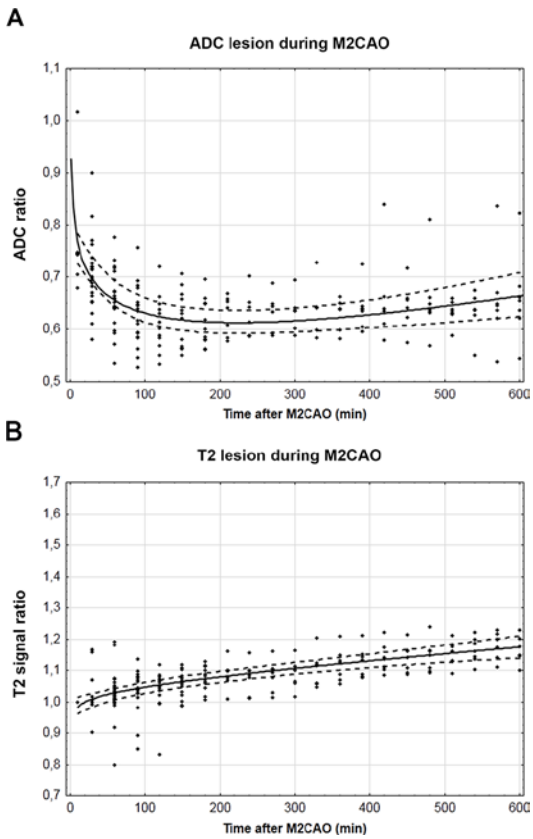

Figure 11. The emergence and progression of ischemic injury. Apparent diffusion coefficient (ADC) and T2 signal ratios between regions of interest and control regions (y-axes), measured at subsequent time points (x-axes) during M2 occlusion (M2CAO)(A, B). Individual data points (diamonds); Equation trend lines (solid lines); confidence intervals (dotted lines).

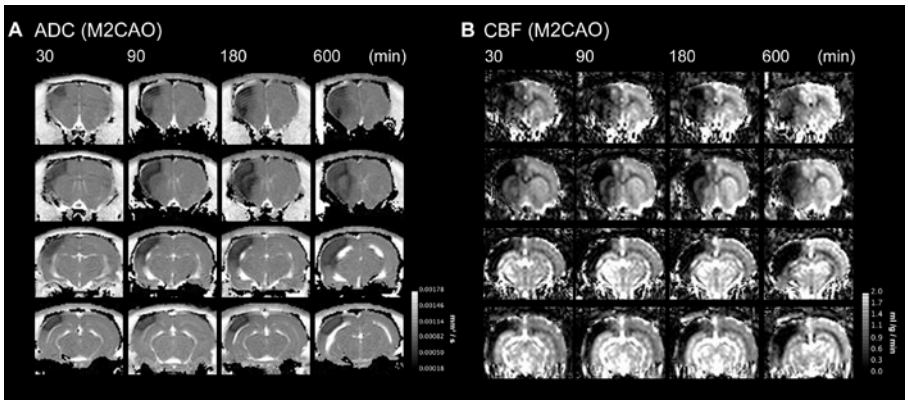

Figure 12. Tissue injury progression during occlusion of the M2 segment of the MCA (M2CAO). Apparent diffusion coefficient (ADC) maps (mm2/s) (A) and cerebral blood flow (CBF) maps (ml/g/min) (B), of four sections from a single animal at 30, 90, 180 and 600 min of M2CAO. At 30 min M2CAO, an ischemic core is already apparent. The lesions volume increases at subsequent time points. The expansion of the ischemic core occurs at the expense of the region of diffusion/perfusion mismatch. However, not even at 600 min does the ischemic lesion encompass the entirety of the perfusion deficit.

4.3 Paper III

The aim of paper III was to employ oxygen-sensitive MRI to identify ischemic regions with increased OEF in order to delineate the ischemic penumbra. We used DWI to outline the ischemic core, and measured the volume of the ischemic core-OEF elevation (IC-OEF) mismatch. We also measured the volume of DWI/PWI mismatch (IC-CBF) in the same animals. The volume of the of the IC-OEF mismatch was compared to, and found to be significantly smaller than the IC-CBF mismatch (Figure 13). The OEF of the IC-OEF mismatch was 90%, while the OEF of the healthy contra lateral control region was 40%.

We further analyzed OEF and $CMRO_2$ levels of tissue subjected to perfusion deficits severe enough to be consistent with tissue at high risk of infarction (12-22 ml/100 g/min), but importantly not yet exhibiting the signs of restricted diffusion which would indicate an emergence of irreversible damage. The tissue was referred to as the penumbra ROI (PEN). When compared to control regions, the PEN had significantly increased OEF levels and $CMRO_2$ levels that, although significantly reduced, did not fall below the threshold for infarction at 65 µmol /100 g/min(*132*). Ischemic core regions also exhibited increased OEF during M2CAO. Reperfusion caused the normalization of OEF in both the ischemic core and the penumbra, emphasizing the potential of fast revasculatory treatment to achieve significant neurological recovery in AIS (Figure 14).

4.3.1 BOLD MRI may provide increased penumbra specificity

The metabolic MRI protocol used in paper III was based on a qBOLD model developed by Yablonskiy et al. describing the relationship between R2' relaxation time, venous dHb fraction and CBVv in a network of randomly oriented cylinders(*73*). We combined R2' with the CBV-measuring capacity of T-DASL to calculate OEF maps over regions subjected to M2CAO. We found that the IC-OEF mismatch comprises a significantly smaller tissue volume than the IC-CBF mismatch in the same animals. These results were interpreted as an improvement of penumbra specificity based on several considerations. In human AIS patients, MCA infarct volumes resulting from large vessel occlusion commonly manifest at 4.5-14% of the hemispheric volume(*125, 140*). This matches the infarct volumes produced by M2CAO where mean infarct sizes are usually around 10% of the hemispheric volume. Results presented in paper II have shown us how the rate of irreversible damage expansion, although initially rapid, subsequently slows down and does not, even after 10 h M2CAO, encompass the entirety of the DWI/PWI mismatch region.

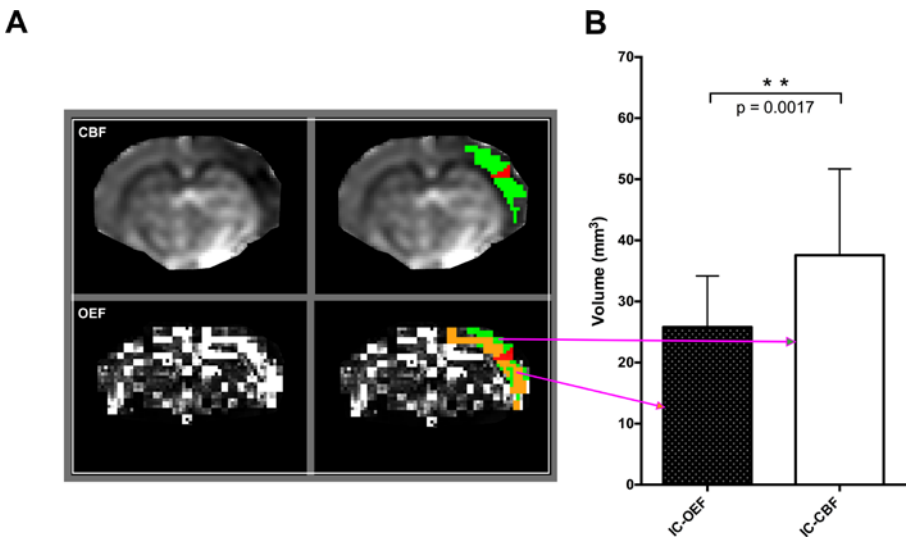

Figure 13. Volumetric Comparison of mismatch regions during M2CAO.
A: Examples of Regions of Interest from a single animal. Cerebral Blood Flow (CBF) and Oxygen Extraction Fraction (OEF) maps (left column). The Ischemic Core (red) was segmented in Apparent Diffusion Coefficient maps. The IC-CBF mismatch ROI (green) was defined as viable regions, with decreased CBF (top of the right column). The IC-OEF mismatch (orange) was defined as viable regions with an apparent OEF elevation (bottom of the right column). B: The volume of the IC-OEF mismatch was significantly smaller than the volume of the IC-CBF mismatch.

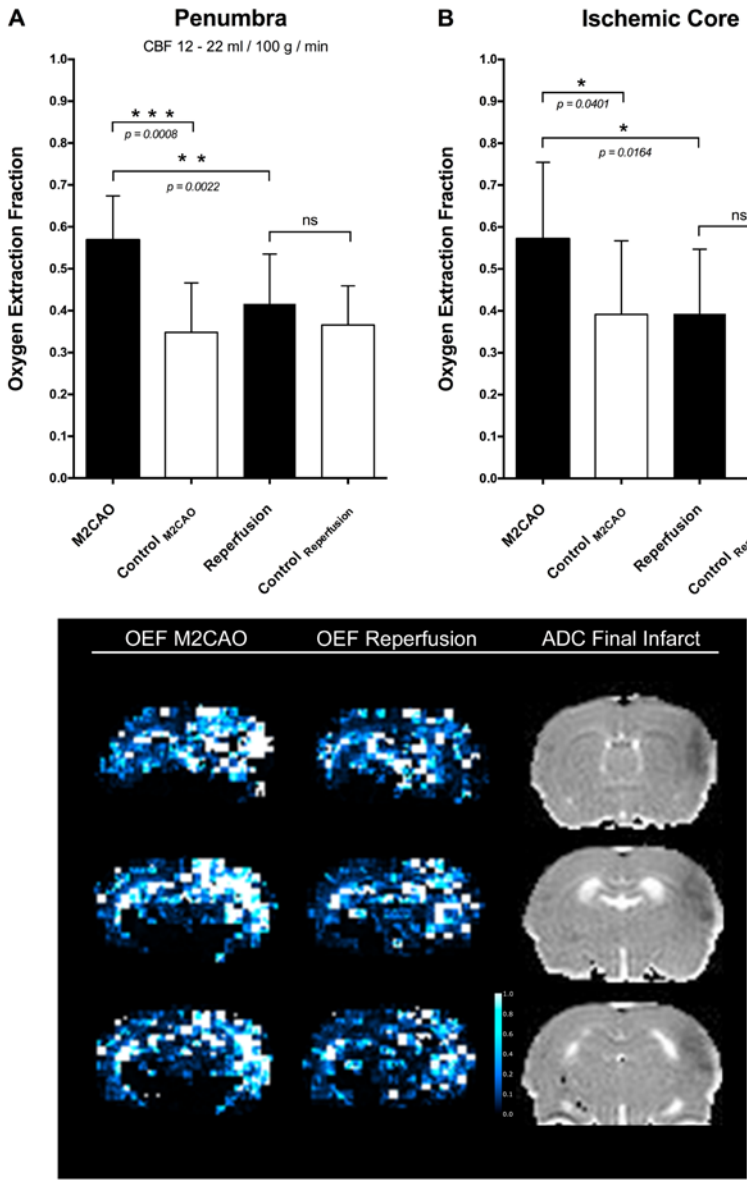

Figure 14. The oxygen extraction fraction (OEF) in ischemic regions during M2 occlusion (M2CAO) and after the restoration of blood flow (reperfusion). Top panel: Increased OEF occurred in the penumbra (A), and in the ischemic core (B) during M2CAO but normalized after reperfusion. The lower panel shows three axial slices from the same animal. Increased OEF is present in regions surrounding the infarct lesion (right column) during M2CAO. Reperfusion results in OEF normalization (middle column).

We conclude from this that a significant portion of the IC-CBF mismatch does not consist of tissue at an immediate risk of infarction. In view of these findings, a more spatially restricted outline of the ischemic penumbra would appear appropriate, especially when taken into account that results from human AIS patients have shown the DWI lesion to make up just 30% of the of the PWI deficit volume when examined at 10 h after symptom onset(*56*). Furthermore, results presented in this study show how severely hypoperfused yet still viable tissue (CBF 12–22ml/100 g/min) exhibits the metabolic adjustments, i.e increased OEF, necessary to sustain the $CMRO_2$ levels needed for the continued viability of brain tissue(*141*). These results correspond well to previous results from DWI-PWI mismatch and peri-infarct regions studied with ^{15}O PET in human patients(*42, 64, 142*), as well as in experimental studies using animal stroke models of MCA occlusion(*39, 143, 144*).

It should be mentioned also, that while OEF elevation in the ischemic penumbra has been previously described in studies employing gold standard ^{15}O studies, in paper III, we observed increased OEF in regions suffering restricted diffusion. This documented increased in OEF in IC regions lends support to the view that fractions of the cells that make up regions with restricted diffusion actually remain metabolically active as they accumulate cytotoxic edema. Does a significant fraction of the ADC lesion represent tissue that exists in the last phase of penumbra before undergoing destruction, and may this tissue be salvageable? This is a worthwhile hypothesis for future studies. In conclusion, the development of metabolic imaging regimens akin to IC-OEF mismatch are motived by the potential gains of obtaining measurements of tissue status in the acute and subacute phases of ischemic stroke as well as in CCH.

4.3.2 Potential improvements

The examination of oxygen metabolism with qBOLD is limited by the need to combine several MRI techniques. We used MEMS and MGE3D to derive R2′, as well as continuous ASL and T-DASL to calculate the hemodynamic parameters of CBF and CBVv, respectively. Out of these methods T-DASL derived CBVv is the limiting factor in terms of spatial resolution and SNR. CBV levels were derived from the difference between the T-DASL signal in the presence and absence of vascular suppression. The relative uncertainty of CBV measurements thereby increases when the T-DASL signal is decreased. One would thus anticipate increased relative uncertainty in CBV in regions with low CBF. Put simply, the method would not work if there was no perfusion. Albeit the PEN ROIs had the lowest CBF and would be most susceptible to low SNR, the mean standard deviation within the penumbra ROIs was only approximately 0.025, which is a worst case estimate of the voxel wise uncertainty if there were no genuine CBV

variations within the penumbra region. In voxels with higher CBF, a lower CBV uncertainty is expected. On a group level, OEF was

consistently lower in control ROIs, while the OEF was elevated in regions with decreased CBF. Moreover, both OEF and the CBF moved toward normalization upon reperfusion. If random noise would dominate CBV measurements, this consistent pattern

would not be observed. In using T-DASL to calculate CBVv we were aware that SNR is inadequate to achieve the absolute OEF or CMRO2 values necessary to determine absolute penumbra thresholds. Accordingly, no such conclusions were presented in paper III. Despite the limitations of T-DASL, however, CBV values acquired in healthy control regions were in line those found in the literature(*78, 145*).We conclude that the SNR of OEF is limited mainly by the SNR in CBVv, rather than the SNR in R2'. Future improvements of the methodology employed in paper III should focus on obtaining a more sensitive method to measure CBVv.

4.4. Paper IV

4.4.1 [18F]FMISO PET is sensitive to cellular hypoxia in AIS

All but one of animal examined with [18F]FMISO PET exhibited apparent and localized uptake increase within the cortical part of the hemisphere subjected to M2CAO (Figure 15, top panel). The mean volume of regions exhibiting increased [^{18}F]FMISO activity was 90 ± 70 mm^2. This size is considerably larger than the typical size of ischemic lesions produced by the M2CAO model, which is usually in the range of 20-30 mm^2. No apparent or localized increase in [^{64}Cu]CuATSM uptake could be found in the M2CAO cortex of examined animals, not even when guided by ADC-maps outlining ischemic lesions with restricted diffusion. Our results thereby do not encourage the use of [^{64}Cu]CuATSM in AIS research. [^{64}Cu]CuATSM is likely better suited for use in oncological imaging where the typical magnitude of hypoxia is more severe than in ischemic stroke.

4.4.2 Hypoxia vulnerability of neurons and astrocytes

IHC analysis revealed decreased amounts of GFAP+ astrocytes within hypoxic regions as defined by pimonidazole uptake (Figure 15, bottom panel, A) in a majority of the animals. No comparable decrease was seen in the population of NeuN+ neurons. The decrease in GFAP+ astrocytes was typically seen in an area smaller than the totality of the hypoxic region. The astrocytes and neurons located in hypoxic regions exhibited significantly higher levels of pimonidazole intensity than cells of corresponding cell types contained in contra lateral control regions. The loss of GFAP + astrocytes in hypoxic core regions has previously been correlated

to cell death(*146, 147*). Such regions are without question headed for infarction considering that neurons cannot survive without astrocytes in close proximity. To determine the respective levels of hypoxia of neurons and astrocytes, we measured the intensity ratios of pimonidazole in neurons and astrocytes by normalizing against non-hypoxic cells of corresponding cell types located in the control region. We found significantly higher pimonidazole intensities in neurons than in astrocytes. These results support the proposition that astrocytes are more sensitive to hypoxia than neurons, considering that astrocytes appear to undergo destruction prior to suffering the relative levels of hypoxia seen in neurons (144, 145).

While the sensitivity of [^{18}F]FMISO to hypoxic tissue is well documented, its penumbra specificity remains unknown. Results presented in paper IV demonstrated a dearth of GFAP+ astrocytes in hypoxic core areas while astrocytes were still present in the periphery of the hypoxic region. We conclude from these results that although [^{18}F]FMISO uptake does identify viable, hypoxic tissue, it may also be present in irreversibly damaged regions. [^{18}F]FMISO should thereby be used in conjunction with an imaging modality capable of identifying the ischemic core, such as CT or DWI MRI. Such examinations will be possible using hybrid systems such as MRI/PET and CT/PET(*148*).

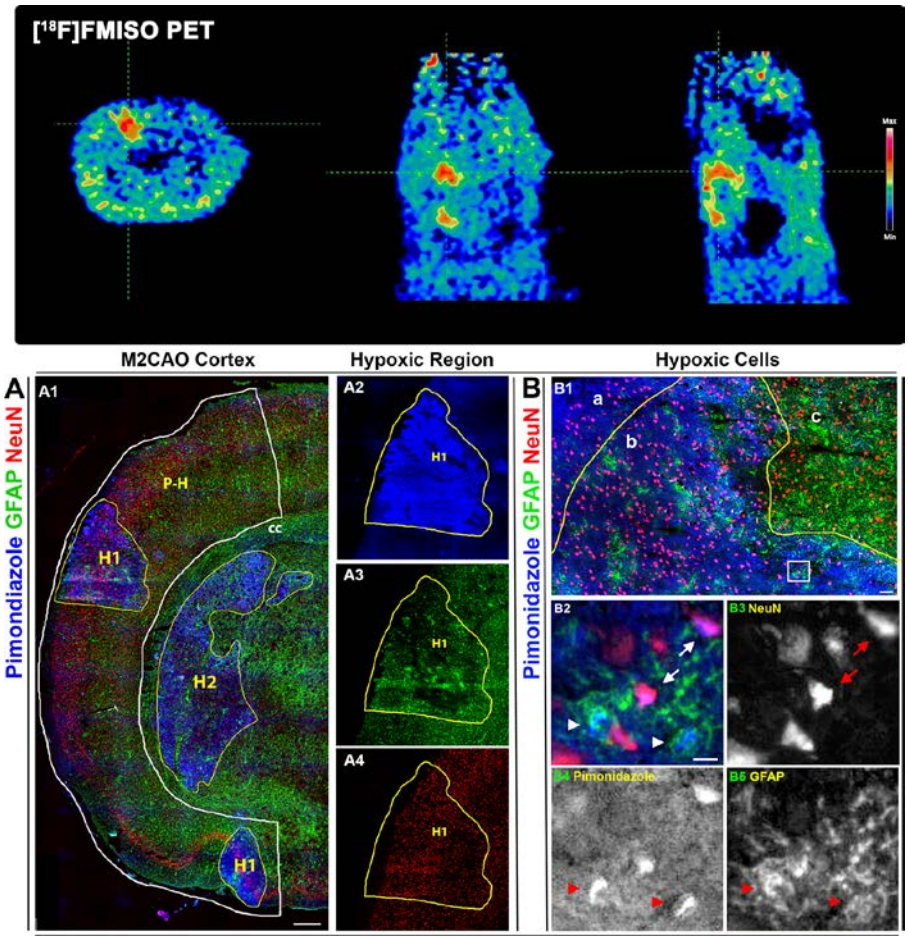

Figure 15. Top panel: [^{18}F]FMISO examination of a single animal during M2CAO; axial (left image), coronal (middle) and sagittal (right) projections. A focal area of increased [^{18}F] FMISO uptake is apparent in the cortex subjected to M2CAO. Lower panel: A1: M2CAO cortex delineated by white line. Pimonidazole (blue, A2), GFAP+ astrocytes (green, A3) and NeuN+ neurons (red, A4). There is a loss of astrocytes in the core of the hypoxic region as seen in H1. P-H: M2CAO cortex without clear pimonidazole uptake. H2: hypoxic region inside the striatum. B1: The loss of astrocytes is apparent in the core of a hypoxic region (a). Although still present, there is a diminished presence of astrocytes, as well as an increased concentration of pimonidazole+ astrocytes and neurons in the border area of the hypoxic region (b) when compared to tissue outside of the hypoxic region (c). B2-B5 (magnification of the white square in B1): Hypoxic astrocytes (arrowheads) and neurons (arrows). Scale bars: A1: 500 μm, B1: 50 μm, B2-B5: 10 μm.

5. CONCLUSIONS

(I) [^{11}C]PBR28 is a suitable radiotracer with which to monitor the progression of neuroinflammation during AIS as modelled by M2CAO.

(II) In AIS as modelled by M2CAO, there is a rapid emergence of an ischemic lesion. However, the subsequent spread of infarction at the expense of the surrounding hypoperfused tissue is slow, and continues for many hours after arterial occlusion. Not all tissue contained in the DWI/PWI mismatch is at risk of infarction.

(III) When combined with DWI, oxygen metabolism MRI provides increased penumbra specificity when compared to the DWI/PWI mismatch. Oxygen metabolism MRI seems well suited for applications in subacute and slow-progressing AIS and CCH.

(IV) Although limited by its substantial accumulation time, if combined with a DWI or CT, [^{18}F]FMISO PET may be a valuable instrument for the identification of tissue-at-risk in subacute ischemic stroke and in cases of CCH. Astrocytes are likely to be more sensitive to hypoxia than neurons in the hyperacute phase of AIS. [^{64}Cu]CuATSM does not appear suited for the identification of tissue-at-risk in AIS.

6. FUTURE PERSPECTIVES

Recent decades have seen the emergence of various imaging-methods attempting to provide reliable identification of the ischemic penumbra through hemodynamic and metabolic read-outs. The ambition has been to locate an adequate intersection between accuracy and clinical availability; however, attempts to improve penumbra specificity have come at the expense of translational potential. In order to overcome this junction, the question should be asked as to what is required of imaging techniques in order to make them suitable for clinical application. With irreversible brain injury in most AIS cases progressing rapidly during severe ischemia, the necessity of short examination times is not in question. Revasculatory treatment must not be delayed by unnecessary imaging. A reasonably accurate estimate of the volume of infarct is needed, motivated by the fact that this is the relevant parameter when assessing the risk of a hemorrhage or other complications resulting from the treatment. In order to motivate treatment in the first place, a measurement of potentially salvageable tissue must also be obtained. Since 2015, the beneficial effects of mechanical thrombectomy when supported by diagnostic imaging has been shown in several randomized trials(*4*). Imaging protocols such as CT perfusion and MRI DWI/PWI mismatch are capable of identifying patients suitable for treatment on the basis of limited infarctions and large regions exhibiting hypoperfusion(*149*). The resurrection of blood flow to salvageable tissue may in best-case scenarios restore full health to AIS patients, providing that the therapeutic intervention occurs early enough, as *time is brain*. Does that mean that the time from the last-known-well is in itself adequate for the triage of individual patients? The answer is no, and for several reasons; for one, a substantial proportion of AIS cases occur during sleep, rendering the time of onset highly uncertain. Even in patients who are awake when ictus occurs the onset of symptoms may not accurately correspond to the time of vascular occlusion. In addition, the rate of infarct progression is heterogeneous between patients. While *the time is brain* paradigm is suitable during the initial hours after ictus, a substantial number of patients will not receive recanalizing treatment because they arrive at hospital after the time-window indicating acute intervention, or because they have an uncertain time of onset. There are now an increasing number of clinical observations proposing the potential of penumbra viability beyond the short, hyperacute phase of AIS. The DAWN trial showed the benefits of delayed thrombectomy in patients with limited ischemic lesions in conjunction with a clinical presentation indicating the presence of functionally impaired, i.e. penumbral, tissue as long as 24 h after ictus(*7*). The DEFUSE 3 trial presented similar results but up to 16 h after ictus in patients with large hypoperfused regions as well as limited detectable infarcts using CT or MRI(*8*). The prospect of prolonged penumbra viability encourages the development and implementation of imaging techniques capable of directly assessing tissue status rather than indirect measurements such as PWI when handling the substantial proportion (30%) of large vessel AIS patients who

suffer slow-progressing infarcts, and who arrive at hospital beyond the initial 6 h of AIS(*150, 151*). The uncertainty inherent to PWI will be increased in these patients, considering that survival time of ischemic tissue-at-risk is determined both by the duration and the severity of a perfusion deficit. In addition, patients presenting with arterial neck dissections and incomplete circle of Willis sometimes exhibit symptoms consistent with CCH, as do patients with advanced chronic atherosclerotic lesions either proximal or distal to the circle of Willis. In these patients it is often challenging to determine whether the symptoms are due to hypoperfusion or not, and if the potential benefits of revasculatory treatment outweigh the associated risks. Clinical decision-making would thereby be facilitated by diagnostic imaging capable of increased penumbra specificity. In this context, metabolic MRI, as well as hypoxia PET are viable candidates to improve stroke health care by enhancing penumbra specificity in the subacute phase and in CCH where slightly longer examination times are not as detrimental to the individual patient. Although it is the case that several of the imaging techniques used in experimental research have little immediate potential for large-scale clinical translation, they remain valuable for the validation and improvement of more readily available methods. In fact, MRI as well as PET continue to contribute substantially to the understanding of pathophysiological processes both in the context of acute ischemia and in the chronic phase when secondary injury mechanism such as neuroinflammation impact on clinical outcome. The translational potential of experimental research consistently improves with technical advancements such as the emergence of hybrid systems capable of simultaneous PET/MRI or PET/CT examinations. Technological advances include the implementation of novel radiotracers designed to better visualize ischemic injury and the neuroinflammatory response following AIS(*152, 153*). The continuing focus on methods for in-vivo imaging of AIS-associated disease processes in experimental research is warranted by the potential to improve the diagnostic regimes currently used in clinical settings, and by the need to ensure that proposed neuroprotective and neurorestorative treatment strategies can be accurately evaluated. This is especially relevant in the field of neuroinflammation, where pharmacological agents capable of modulating the inflammatory response may in the future reduce the neurological deficits suffered by stroke patients.

In conclusion, Protocols akin to the metabolic MRI described in this thesis should be improved by shorter examination times and increased SNR. As with PET hypoxia imaging, it is crucial that their capability to identify penumbra is validated against ^{15}0 PET in human stroke patients. If successful, metabolic MRI as well as PET hypoxia imaging may provide increased diagnostic power especially pertinent to the subacute phase of stroke as well as in CCH where determining tissue status may be more appropriate than counting the hours since the last-known-well. Future studies on AIS imaging should focus also on clarifying whether fractions of regions exhibiting restricted diffusion, currently considered to be irreversibly damaged, may in fact be salvageable in the very early phase of AIS.

7. ACKNOWLEDGEMENTS

A thesis has many mothers and fathers. I wish to express my gratitude,

To **Staffan Holmin**. Thank you for the opportunity to write this thesis, and for the tremendous support along the way. You have the sharp and humble mind of a true researcher. Thanks for trusting me, for letting me make mistakes, and for pushing me to improve. Every PhD student undertakes his or her own journey, which for me was also a journey into adulthood. Thank you for being an excellent role model.

To **Peter Damberg**. You are the Yoda of MRI, and a very good guy. This thesis had not been possible without your immense contribution.

To **Michael Söderman** and **Tommy Andersson**. Thank you for your expertise on acute ischemic stroke.

To **Jan Mulder.** With characteristic Dutch directness, you have contributed immeasurably to the work contained in this thesis. Also, you were probably the only person involved in this project with whom I could really talk about football.

To every person in my research group. You are great.

To **Fabian Arnberg**, for taking me under your wing when I first showed up at the lab and for teaching me the M2CAO model with kindness and patience. You always had time for me, even when I called you at midnight to fret about my experiments. Thank you for providing support akin to that of a big brother. You always pointed me in the right direction.

To **Johan Lundberg**, the great renaissance man, for your help, advice and support. I remember drinking fresh mint tea with you next to the Medusa heads in the Basilica cistern in Istanbul. That was cool.

To **Stefan Jonsson.** Thank you for many interesting discussions, on everything from smart metals to affairs of the heart. Thank you especially for your kindness and optimism.

To **Rikard Grankvist**, you are kind, helpful, intelligent and probably the hardest worker I´ve met. The fact that as medical students, we both received a scolding from the same eminent professor makes me smile. I think we´ve done alright since then. Thank you for great company over the years.

To **Arvin** big-data **Chireh**, you have the brains and skill to go far. I will never forget when you told me that “A fool can throw a stone in a pond that a hundred wise men cannot get out”. You were right.

To **Petra Brinkestål**. Your help with difficult tasks made my life so much easier. Good luck in the future.

To **Ida Jonsson**, your energy and work rate has been inspiring. Nobody plans a one-day excursion more efficiently than you.

To **Victoria Lövljung**. You have a versatile and measured mind. Thank you for energizing discussions on career paths, money and wellness.

To **Mikael Sandell**. Thank you for being a brilliant and friendly guy. Will you one day sit on Professor Jonssons smart metal throne?

To **Vamsi Gontu**. You are one of the nicest people I´ve met, as well as being a thoroughly clever and dedicated PhD student.

To **Håkan Almqvist**. It´s been a privilege. Thank you for answering a hundred and one questions with cheery authority when we worked together in the clinic.

To **Leonard Yeo**. I´ve never had as much fun working with anyone as I had with you. You brought international pizzazz to the lab.

To **Li Lu, Erik Samén, Emma Jussing**, **Jonas Grafström, Thuy Tran**, **Tanya Tegnebratt** and last but not least, Professor Emeritus **Sharon Stone-Elander** (America was always great): Thank you all for letting me borrow your PET-scanner and for explaining what I was supposed to do. I owe special thanks to you **Li** for your exceptional ability to perform animal procedures.

To the many people who have significantly helped me in completing this thesis; **Anki Sandberg-Nordqvist** and **Pellina Janson,** your good-cop bad-cop double act is unparalleled**.** Anki, thank you for keeping faith in me. Pellina, thank you, I will miss the early morning banter. Thank you both, as well as Kicki Edvardsson, for maintaining the formidable infrastructure and professionalism at KERIC.

Kicki Edvardsson, Sahar Nikkhou-Aski, Sara Lundqvist, Susanna Nevala, Patrik Jarvoll, Zsolt Sarnyai, Nasreen Jaff, Ann-Marie Mikkola, Irja Eggertsen, Aga Limiszewska. Without the structure and competence that you have provided this project would have been a non-starter.

Miklós Tóth, Balázs Gulyás, Ola Kvist and Sandra Kraft. Thank you for your excellent work in our collaborations and for being formidable human beings. **To Gustav Nilsonne** , you are a genuine gentleman. Thank you for giving me my first gig in research. **To Nicholas Mitsios**, thank you for your help in performing immunohistochemistry, and for telling me about the many islands of Greece. To **Magnus Kaijser**, for a shared love of London, for taking an interest in my research,

and for giving me the chance to try my hand at clinical neuroradiology. To **Eric Thelin**, **Samuel Röhl**, **Cyril Monnot, Adam Sierakowiak and Lora Weidner;** thank you for letting me exchange ideas with great and fellow PhD-students.

To **Britt-Marie** and **Frank Little**, mum and dad. Thank you for the kindness, love and support of a lifetime. This thesis has its roots in Stockholm and Liverpool (COYB!). I am a fortunate son. To **Robin Little**, my special and wonderful brother.

To grand-parents, uncles, aunts, cousins; **Gunnar Gustafsson, Ethel Gustafsson, Francis Little, Catherine Little, Hans-Gunnar Gunnarsson, Ingrid Gunnarsson, Peter Gunnarsson, Karin Gunnarsson, Kathleen Little, Tony Little, Claire Jones, Sarah Little, Joseph Little, Anneli Uggla, Marcus Uggla, John Uggla, Carl Uggla, Antti Uotinen, Helena Uotinen, Marianne Uotinen, Katarina Uotinen**. Thank you for providing my foundations.

To **Gabriel Nordenankar**, **Theodore Ripman**, **Martin Dalaryd**, **Erik Billving**, **Patrik Balint and James Powell**. Thank you for decades of friendship. To **Magnus Ahlbom,** for exceptional comradeship since we began our medical studies together.

To **Roland Roberts, Wivi-Anne Roberts, Rhianwen Roberts, Ales Jerman and the extended Roberts family**; **Trevor Roberts, Enid Roberts, Julia Alexander, Caroline Roberts, David Roberts, Claire Roberts**. You are a great bunch. Thank you for your friendship and support, and for showing me Marylebone and the Lake District.

Tudor, thank you for taking me out on walks around Djurgården on Saturday afternoons. It really cleared my mind.

And finally, to darling **Ceridwen**, my English rose and the rock of my life. Nothing would have been possible without you. Living with you is a belter. You are entirely beloved.

People say I'm lazy
Dreaming my life away
Well they give me all kinds of advice
Designed to enlighten me
When I tell them that I'm doing fine watching shadows on the wall
"Don't you miss the big time boy, you're no longer on the ball?"

- John Lennon, *Watching the Wheels*

REFERENCES

1. G. J. Hankey, Stroke. *Lancet* **389**, 641-654 (2017).
2. J. M. Wardlaw, Neuroimaging in acute ischaemic stroke: insights into unanswered questions of pathophysiology. *J Intern Med* **267**, 172-190 (2010).
3. K. Malhotra, D. S. Liebeskind, Imaging in Endovascular Stroke Trials. *J Neuroimaging* **25**, 517-527 (2015).
4. B. K. Menon, B. C. Campbell, C. Levi, M. Goyal, Role of imaging in current acute ischemic stroke workflow for endovascular therapy. *Stroke* **46**, 1453-1461 (2015).
5. W. D. Heiss, The ischemic penumbra: how does tissue injury evolve? *Ann N Y Acad Sci* **1268**, 26-34 (2012).
6. M. Goyal *et al.*, Endovascular thrombectomy after large-vessel ischaemic stroke: a meta-analysis of individual patient data from five randomised trials. *Lancet* **387**, 1723-1731 (2016).
7. R. G. Nogueira *et al.*, Thrombectomy 6 to 24 Hours after Stroke with a Mismatch between Deficit and Infarct. *N Engl J Med* **378**, 11-21 (2018).
8. G. W. Albers *et al.*, Thrombectomy for Stroke at 6 to 16 Hours with Selection by Perfusion Imaging. *N Engl J Med* **378**, 708-718 (2018).
9. A. Ciacciarelli, G. Sette, F. Giubilei, F. Orzi, Chronic cerebral hypoperfusion: An undefined, relevant entity. *J Clin Neurosci*, (2020).
10. K. Nael *et al.*, Six-minute magnetic resonance imaging protocol for evaluation of acute ischemic stroke: pushing the boundaries. *Stroke* **45**, 1985-1991 (2014).
11. P. V. Little, S. E. Kraft, A. Chireh, P. Damberg, S. Holmin, Oxygen metabolism MRI - A comparison with perfusion imaging in a rat model of MCA branch occlusion and reperfusion. *J Cereb Blood Flow Metab*, 271678X19892271 (2019).
12. J. Astrup, B. K. Siesjö, L. Symon, Thresholds in cerebral ischemia - the ischemic penumbra. *Stroke* **12**, 723-725 (1981).
13. J. L. Saver *et al.*, Time to Treatment With Endovascular Thrombectomy and Outcomes From Ischemic Stroke: A Meta-analysis. *JAMA* **316**, 1279-1288 (2016).
14. J. C. Baron, T. Jones, Oxygen metabolism, oxygen extraction and positron emission tomography: Historical perspective and impact on basic and clinical neuroscience. *Neuroimage* **61**, 492-504 (2012).

15. S. Jung *et al.*, Relevance of the cerebral collateral circulation in ischaemic stroke: time is brain, but collaterals set the pace. *Swiss Med Wkly* **147**, w14538 (2017).

16. W. J. Powers, Cerebral hemodynamics in ischemic cerebrovascular disease. *Ann Neurol* **29**, 231-240 (1991).

17. J. C. Baron *et al.*, Reversal of focal "misery-perfusion syndrome" by extra-intracranial arterial bypass in hemodynamic cerebral ischemia. A case study with 15O positron emission tomography. *Stroke* **12**, 454-459 (1981).

18. Y. Morita *et al.*, Rapid changes in pial arterial diameter and cerebral blood flow caused by ipsilateral carotid artery occlusion in rats. *Keio J Med* **46**, 120-127 (1997).

19. K. A. Hossmann, Pathophysiology and therapy of experimental stroke. *Cell Mol Neurobiol* **26**, 1057-1083 (2006).

20. G. A. Armitage, K. G. Todd, A. Shuaib, I. R. Winship, Laser speckle contrast imaging of collateral blood flow during acute ischemic stroke. *J Cereb Blood Flow Metab* **30**, 1432-1436 (2010).

21. C. Howarth, P. Gleeson, D. Attwell, Updated energy budgets for neural computation in the neocortex and cerebellum. *J Cereb Blood Flow Metab* **32**, 1222-1232 (2012).

22. U. Jensen-Kondering, J. C. Baron, Oxygen imaging by MRI: can blood oxygen level-dependent imaging depict the ischemic penumbra? *Stroke* **43**, 2264-2269 (2012).

23. S. Currie, N. Hoggard, I. J. Craven, M. Hadjivassiliou, I. D. Wilkinson, Understanding MRI: basic MR physics for physicians. *Postgrad Med J* **89**, 209-223 (2013).

24. R. Bitar *et al.*, MR pulse sequences: what every radiologist wants to know but is afraid to ask. *Radiographics* **26**, 513-537 (2006).

25. T. G. Turkington, Introduction to PET instrumentation. *J Nucl Med Technol* **29**, 4-11 (2001).

26. C. S. Levin, Primer on molecular imaging technology. *Eur J Nucl Med Mol Imaging* **32 Suppl 2**, S325-345 (2005).

27. W. D. Heiss, Malignant MCA Infarction: Pathophysiology and Imaging for Early Diagnosis and Management Decisions. *Cerebrovasc Dis* **41**, 1-7 (2015).

28. T. Neumann-Haefelin *et al.*, Serial MRI after transient focal cerebral ischemia in rats: dynamics of tissue injury, blood-brain barrier damage, and edema formation. *Stroke* **31**, 1965-1972; discussion 1972-1963 (2000).

29. O. Abe *et al.*, MR imaging of ischemic penumbra. *Eur J Radiol* **46**, 67-78 (2003).

30. M. E. Moseley *et al.*, Early detection of regional cerebral ischemia in cats: comparison of diffusion- and T2-weighted MRI and spectroscopy. *Magn Reson Med* **14**, 330-346 (1990).

31. G. P. Winston, The physical and biological basis of quantitative parameters derived from diffusion MRI. *Quant Imaging Med Surg* **2**, 254-265 (2012).

32. K. W. Muir, A. Buchan, R. von Kummer, J. Rother, J. C. Baron, Imaging of acute stroke. *Lancet Neurol* **5**, 755-768 (2006).

33. O. B. Paulson, N. A. Lassen, E. Skinhoj, Regional cerebral blood flow in apoplexy without arterial occlusion. *Neurology* **20**, 125-138 (1970).

34. T. S. Olsen, B. Larsen, M. Herning, E. B. Skriver, N. A. Lassen, Blood flow and vascular reactivity in collaterally perfused brain tissue. Evidence of an ischemic penumbra in patients with acute stroke. *Stroke* **14**, 332-341 (1983).

35. M. M. Ter-Pogossian, J. O. Eichling, D. O. Davis, M. J. Welch, The measure in vivo of regional cerebral oxygen utilization by means of oxyhemoglobin labeled with radioactive oxygen-15. *J Clin Invest* **49**, 381-391 (1970).

36. T. Jones, D. A. Chesler, M. M. Ter-Pogossian, The continuous inhalation of oxygen-15 for assessing regional oxygen extraction in the brain of man. *Br J Radiol* **49**, 339-343 (1976).

37. G. L. Lenzi, T. Jones, C. G. McKenzie, S. Moss, Non-invasive regional study of chronic cerebrovascular disorders using the oxygen-15 inhalation technique. *J Neurol Neurosurg Psychiatry* **41**, 11-17 (1978).

38. R. H. Ackerman *et al.*, Positron imaging in ischemic stroke disease using compounds labeled with oxygen 15. Initial results of clinicophysiologic correlations. *Arch Neurol* **38**, 537-543 (1981).

39. W. D. Heiss *et al.*, Dynamic penumbra demonstrated by sequential multitracer PET after middle cerebral artery occlusion in cats. *J Cereb Blood Flow Metab* **14**, 892-902 (1994).

40. W. D. Heiss, G. Rosner, Functional recovery of cortical neurons as related to degree and duration of ischemia. *Ann Neurol* **14**, 294-301 (1983).

41. A. M. Hakim *et al.*, The effect of nimodipine on the evolution of human cerebral infarction studied by PET. *J Cereb Blood Flow Metab* **9**, 523-534 (1989).

42. R. J. Wise, S. Bernardi, R. S. Frackowiak, N. J. Legg, T. Jones, Serial observations on the pathophysiology of acute stroke. The transition from ischaemia to infarction as reflected in regional oxygen extraction. *Brain* **106 (Pt 1)**, 197-222 (1983).

43. W. D. Heiss, G. R. Fink, M. Huber, K. Herholz, Positron emission tomography imaging and the therapeutic window. *Stroke* **24**, I50-53; discussion I48-59, I54-56 (1993).

44. N. M. Alpert *et al.*, Measurement of rCBE and rCMRO2 by continuous inhalation of 15O-labeled CO2 and O2. *Acta Neurol Scand Suppl* **64**, 186-187 (1977).

45. R. S. Frackowiak, G. L. Lenzi, T. Jones, J. D. Heather, Quantitative measurement of regional cerebral blood flow and oxygen metabolism in man using 15O and positron emission tomography: theory, procedure, and normal values. *J Comput Assist Tomogr* **4**, 727-736 (1980).

46. J. C. Baron *et al.*, Use of PET methods for measurement of cerebral energy metabolism and hemodynamics in cerebrovascular disease. *J Cereb Blood Flow Metab* **9**, 723-742 (1989).

47. A. A. Lammertsma, T. Jones, Correction for the presence of intravascular oxygen-15 in the steady-state technique for measuring regional oxygen extraction ratio in the brain: 1. Description of the method. *J Cereb Blood Flow Metab* **3**, 416-424 (1983).

48. L. Ostergaard, R. M. Weisskoff, D. A. Chesler, C. Gyldensted, B. R. Rosen, High resolution measurement of cerebral blood flow using intravascular tracer bolus passages. Part I: Mathematical approach and statistical analysis. *Magn Reson Med* **36**, 715-725 (1996).

49. L. Ostergaard *et al.*, High resolution measurement of cerebral blood flow using intravascular tracer bolus passages. Part II: Experimental comparison and preliminary results. *Magn Reson Med* **36**, 726-736 (1996).

50. J. A. Detre *et al.*, Tissue specific perfusion imaging using arterial spin labeling. *NMR Biomed* **7**, 75-82 (1994).

51. Y. Meng, P. Wang, S. G. Kim, Simultaneous measurement of cerebral blood flow and transit time with turbo dynamic arterial spin labeling (Turbo-DASL): application to functional studies. *Magn Reson Med* **68**, 762-771 (2012).

52. E. Bandera *et al.*, Cerebral blood flow threshold of ischemic penumbra and infarct core in acute ischemic stroke: a systematic review. *Stroke* **37**, 1334-1339 (2006).

53. A. E. Baird *et al.*, Enlargement of human cerebral ischemic lesion volumes measured by diffusion-weighted magnetic resonance imaging. *Ann Neurol* **41**, 581-589 (1997).

54. R. Markus *et al.*, Hypoxic tissue in ischaemic stroke: persistence and clinical consequences of spontaneous survival. *Brain* **127**, 1427-1436 (2004).

55. S. Warach, J. F. Dashe, R. R. Edelman, Clinical outcome in ischemic stroke predicted by early diffusion-weighted and perfusion magnetic resonance imaging: a preliminary analysis. *J Cereb Blood Flow Metab* **16**, 53-59 (1996).

56. P. A. Barber *et al.*, Prediction of stroke outcome with echoplanar perfusion- and diffusion-weighted MRI. *Neurology* **51**, 418-426 (1998).

57. C. Beaulieu *et al.*, Longitudinal magnetic resonance imaging study of perfusion and diffusion in stroke: evolution of lesion volume and correlation with clinical outcome. *Ann Neurol* **46**, 568-578 (1999).

58. N. Kraemer *et al.*, Magnetic resonance imaging and clinical patterns of patients with 'spectacular shrinking deficit' after acute middle cerebral artery stroke. *Cerebrovasc Dis* **20**, 285-290 (2005).

59. S. Davis *et al.*, Perfusion/Diffusion mismatch is valid and should be used for selecting delayed interventions. *Transl Stroke Res* **3**, 188-197 (2012).

60. G. W. Albers *et al.*, Magnetic resonance imaging profiles predict clinical response to early reperfusion: the diffusion and perfusion imaging evaluation for understanding stroke evolution (DEFUSE) study. *Ann Neurol* **60**, 508-517 (2006).

61. Y. Nagakane *et al.*, EPITHET: Positive Result After Reanalysis Using Baseline Diffusion-Weighted Imaging/Perfusion-Weighted Imaging Co-Registration. *Stroke* **42**, 59-64 (2011).

62. M. G. Lansberg *et al.*, MRI profile and response to endovascular reperfusion after stroke (DEFUSE 2): a prospective cohort study. *Lancet Neurol* **11**, 860-867 (2012).

63. J. L. Saver *et al.*, Stent-retriever thrombectomy after intravenous t-PA vs. t-PA alone in stroke. *N Engl J Med* **372**, 2285-2295 (2015).

64. J. Sobesky *et al.*, Does the mismatch match the penumbra? Magnetic resonance imaging and positron emission tomography in early ischemic stroke. *Stroke* **36**, 980-985 (2005).

65. F. Scalzo, M. Nour, D. S. Liebeskind, Data science of stroke imaging and enlightenment of the penumbra. *Front Neurol* **6**, 8 (2015).

66. J. M. Olivot *et al.*, Hypoperfusion intensity ratio predicts infarct progression and functional outcome in the DEFUSE 2 Cohort. *Stroke* **45**, 1018-1023 (2014).

67. H. M. Wheeler *et al.*, The growth rate of early DWI lesions is highly variable and associated with penumbral salvage and clinical outcomes following endovascular reperfusion. *Int J Stroke* **10**, 723-729 (2015).

68. S. Ogawa, T. M. Lee, A. S. Nayak, P. Glynn, Oxygenation-sensitive contrast in magnetic resonance image of rodent brain at high magnetic fields. *Magn Reson Med* **14**, 68-78 (1990).

69. S. G. Kim, S. Ogawa, Biophysical and physiological origins of blood oxygenation level-dependent fMRI signals. *J Cereb Blood Flow Metab* **32**, 1188-1206 (2012).

70. P. Little *et al.*, Preserved Collateral Blood Flow in the Endovascular M2CAO Model Allows for Clinically Relevant Profiling of Injury Progression in Acute Ischemic Stroke. *PLoS One* **12**, e0169541 (2017).

71. M. Tóth *et al.*, Acute neuroinflammation in a clinically relevant focal cortical ischemic stroke model in rat: longitudinal positron emission tomography and immunofluorescent tracking. *Brain Struct Funct*, (2015).

72. X. He, D. A. Yablonskiy, Quantitative BOLD: mapping of human cerebral deoxygenated blood volume and oxygen extraction fraction: default state. *Magn Reson Med* **57**, 115-126 (2007).

73. D. A. Yablonskiy, E. M. Haacke, Theory of NMR signal behavior in magnetically inhomogeneous tissues: the static dephasing regime. *Magn Reson Med* **32**, 749-763 (1994).

74. N. M. Hirsch *et al.*, Technical considerations on the validity of blood oxygenation level-dependent-based MR assessment of vascular deoxygenation. *NMR Biomed* **27**, 853-862 (2014).

75. D. A. Yablonskiy, A. L. Sukstanskii, X. He, Blood oxygenation level-dependent (BOLD)-based techniques for the quantification of brain hemodynamic and metabolic properties - theoretical models and experimental approaches. *NMR Biomed* **26**, 963-986 (2013).

76. A. S. Gersing *et al.*, Mapping of cerebral metabolic rate of oxygen using dynamic susceptibility contrast and blood oxygen level dependent MR imaging in acute ischemic stroke. *Neuroradiology* **57**, 1253-1261 (2015).

77. A. Seiler *et al.*, The relationship between blood flow impairment and oxygen depletion in acute ischemic stroke imaged with magnetic resonance imaging. *J Cereb Blood Flow Metab* **39**, 454-465 (2019).

78. T. Christen *et al.*, Tissue oxygen saturation mapping with magnetic resonance imaging. *J Cereb Blood Flow Metab* **34**, 1550-1557 (2014).

79. H. An, Q. Liu, Y. Chen, W. Lin, Evaluation of MR-derived cerebral oxygen metabolic index in experimental hyperoxic hypercapnia, hypoxia, and ischemia. *Stroke* **40**, 2165-2172 (2009).

80. A. P. Fan *et al.*, Elevated brain oxygen extraction fraction measured by MRI susceptibility relates to perfusion status in acute ischemic stroke. *J Cereb Blood Flow Metab*, 271678X19827944 (2019).

81. C. Michiels, Physiological and pathological responses to hypoxia. *Am J Pathol* **164**, 1875-1882 (2004).

82. J. C. Walsh *et al.*, The clinical importance of assessing tumor hypoxia: relationship of tumor hypoxia to prognosis and therapeutic opportunities. *Antioxid Redox Signal* **21**, 1516-1554 (2014).

83. R. S. Samraj, L. Nicolas, Near infrared spectroscopy (NIRS) derived tissue oxygenation in critical illness. *Clin Invest Med* **38**, E285-295 (2015).

84. M. Takasawa, R. R. Moustafa, J. C. Baron, Applications of nitroimidazole in vivo hypoxia imaging in ischemic stroke. *Stroke* **39**, 1629-1637 (2008).

85. G. Sette *et al.*, In vivo mapping of brain benzodiazepine receptor changes by positron emission tomography after focal ischemia in the anesthetized baboon. *Stroke* **24**, 2046-2057; discussion 2057-2048 (1993).

86. W. D. Heiss *et al.*, Early detection of irreversibly damaged ischemic tissue by flumazenil positron emission tomography in cats. *Stroke* **28**, 2045-2051; discussion 2051-2042 (1997).

87. W. D. Heiss *et al.*, Permanent cortical damage detected by flumazenil positron emission tomography in acute stroke. *Stroke* **29**, 454-461 (1998).

88. W. D. Heiss *et al.*, Early [(11)C]Flumazenil/H(2)O positron emission tomography predicts irreversible ischemic cortical damage in stroke patients receiving acute thrombolytic therapy. *Stroke* **31**, 366-369 (2000).

89. S. Ejaz *et al.*, Characterizing infarction and selective neuronal loss following temporary focal cerebral ischemia in the rat: a multi-modality imaging study. *Neurobiol Dis* **51**, 120-132 (2013).

90. J. L. Hughes *et al.*, Early-stage. *J Cereb Blood Flow Metab*, 271678X19883040 (2019).

91. A. Nunn, K. Linder, H. W. Strauss, Nitroimidazoles and imaging hypoxia. *Eur J Nucl Med* **22**, 265-280 (1995).

92. S. J. Read *et al.*, Identifying hypoxic tissue after acute ischemic stroke using PET and 18F-fluoromisonidazole. *Neurology* **51**, 1617-1621 (1998).

93. R. Markus *et al.*, Topography and temporal evolution of hypoxic viable tissue identified by 18F-fluoromisonidazole positron emission tomography in humans after ischemic stroke. *Stroke* **34**, 2646-2652 (2003).

94. M. Takasawa *et al.*, Imaging of brain hypoxia in permanent and temporary middle cerebral artery occlusion in the rat using 18F-fluoromisonidazole and positron emission tomography: a pilot study. *J Cereb Blood Flow Metab* **27**, 679-689 (2007).

95. K. Saita *et al.*, Imaging the ischemic penumbra with 18F-fluoromisonidazole in a rat model of ischemic stroke. *Stroke* **35**, 975-980 (2004).

96. H. Saura *et al.*, Hypoxic viable tissue in human chronic cerebral ischemia because of unilateral major cerebral artery steno-occlusive disease. *Stroke* **46**, 1250-1256 (2015).

97. W. D. Heiss, Radionuclide imaging in ischemic stroke. *J Nucl Med* **55**, 1831-1841 (2014).

98. J. A. Alawneh *et al.*, Diffusion and perfusion correlates of the 18F-MISO PET lesion in acute stroke: pilot study. *Eur J Nucl Med Mol Imaging* **41**, 736-744 (2014).

99. Y. Fujibayashi *et al.*, Copper-62-ATSM: a new hypoxia imaging agent with high membrane permeability and low redox potential. *J Nucl Med* **38**, 1155-1160 (1997).

100. P. Bonnitcha, S. Grieve, G. Figtree, Clinical imaging of hypoxia: Current status and future directions. *Free Radic Biol Med* **126**, 296-312 (2018).

101. V. R. Pell, F. Baark, F. Mota, J. E. Clark, R. Southworth, PET Imaging of Cardiac Hypoxia: Hitting Hypoxia Where It Hurts. *Curr Cardiovasc Imaging Rep* **11**, 7 (2018).

102. J. S. Lewis *et al.*, An imaging comparison of 64Cu-ATSM and 60Cu-ATSM in cancer of the uterine cervix. *J Nucl Med* **49**, 1177-1182 (2008).

103. J. L. Tatum *et al.*, Hypoxia: importance in tumor biology, noninvasive measurement by imaging, and value of its measurement in the management of cancer therapy. *Int J Radiat Biol* **82**, 699-757 (2006).

104. K. Tateishi *et al.*, Application of 62Cu-diacetyl-bis (N4-methylthiosemicarbazone) PET imaging to predict highly malignant tumor grades and hypoxia-inducible factor-1α expression in patients with glioma. *AJNR Am J Neuroradiol* **34**, 92-99 (2013).

105. M. G. Handley, R. A. Medina, E. Nagel, P. J. Blower, R. Southworth, PET imaging of cardiac hypoxia: opportunities and challenges. *J Mol Cell Cardiol* **51**, 640-650 (2011).

106. M. Isozaki *et al.*, Feasibility of 62Cu-ATSM PET for evaluation of brain ischaemia and misery perfusion in patients with cerebrovascular disease. *Eur J Nucl Med Mol Imaging* **38**, 1075-1082 (2011).

107. F. C. Barone, G. Z. Feuerstein, Inflammatory mediators and stroke: new opportunities for novel therapeutics. *J Cereb Blood Flow Metab* **19**, 819-834 (1999).

108. G. Raivich *et al.*, Neuroglial activation repertoire in the injured brain: graded response, molecular mechanisms and cues to physiological function. *Brain Res Brain Res Rev* **30**, 77-105 (1999).

109. R. Jin, L. Liu, S. Zhang, A. Nanda, G. Li, Role of inflammation and its mediators in acute ischemic stroke. *J Cardiovasc Transl Res* **6**, 834-851 (2013).

110. G. Stoll, J. W. Griffin, C. Y. Li, B. D. Trapp, Wallerian degeneration in the peripheral nervous system: participation of both Schwann cells and macrophages in myelin degradation. *J Neurocytol* **18**, 671-683 (1989).

111. G. Barreto, R. E. White, Y. Ouyang, L. Xu, R. G. Giffard, Astrocytes: targets for neuroprotection in stroke. *Cent Nerv Syst Agents Med Chem* **11**, 164-173 (2011).

112. T. Mabuchi *et al.*, Contribution of microglia/macrophages to expansion of infarction and response of oligodendrocytes after focal cerebral ischemia in rats. *Stroke* **31**, 1735-1743 (2000).

113. G. Stoll, S. Jander, M. Schroeter, Inflammation and glial responses in ischemic brain lesions. *Prog Neurobiol* **56**, 149-171 (1998).

114. H. Kettenmann, U. K. Hanisch, M. Noda, A. Verkhratsky, Physiology of microglia. *Physiol Rev* **91**, 461-553 (2011).

115. M. V. Sofroniew, H. V. Vinters, Astrocytes: biology and pathology. *Acta Neuropathol* **119**, 7-35 (2010).

116. A. Bonaventura, F. Montecucco, F. Dallegri, Cellular recruitment in myocardial ischaemia/reperfusion injury. *Eur J Clin Invest* **46**, 590-601 (2016).

117. N. A. Flaris, T. L. Densmore, M. C. Molleston, W. F. Hickey, Characterization of microglia and macrophages in the central nervous system of rats: definition of the differential expression of molecules using standard and novel monoclonal antibodies in normal CNS and in four models of parenchymal reaction. *Glia* **7**, 34-40 (1993).

118. P. Rezaie, D. Male, Mesoglia & microglia--a historical review of the concept of mononuclear phagocytes within the central nervous system. *J Hist Neurosci* **11**, 325-374 (2002).

119. W. Y. Chan, S. Kohsaka, P. Rezaie, The origin and cell lineage of microglia: new concepts. *Brain Res Rev* **53**, 344-354 (2007).

120. R. Myers *et al.*, Macrophage and astrocyte populations in relation to [3H] PK 11195 binding in rat cerebral cortex following a local ischaemic lesion. *J Cereb Blood Flow Metab* **11**, 314-322 (1991).

121. D. T. Stephenson *et al.*, Peripheral benzodiazepine receptors are colocalized with activated microglia following transient global forebrain ischemia in the rat. *J Neurosci* **15**, 5263-5274 (1995).

122. S. Rojas *et al.*, Imaging brain inflammation with [(11)C]PK11195 by PET and induction of the peripheral-type benzodiazepine receptor after transient focal ischemia in rats. *J Cereb Blood Flow Metab* **27**, 1975-1986 (2007).

123. Q. Guo, D. R. Owen, E. A. Rabiner, F. E. Turkheimer, R. N. Gunn, Identifying improved TSPO PET imaging probes through biomathematics: the impact of multiple TSPO binding sites in vivo. *Neuroimage* **60**, 902-910 (2012).

124. M. Imaizumi *et al.*, PET imaging with [11C]PBR28 can localize and quantify upregulated peripheral benzodiazepine receptors associated with cerebral ischemia in rat. *Neurosci Lett* **411**, 200-205 (2007).

125. S. T. Carmichael, Rodent models of focal stroke: size, mechanism, and purpose. *NeuroRx* **2**, 396-409 (2005).

126. J. O. Brown, The morphology of circulus arteriosus cerebri in rats. *Anat Rec* **156**, 99-106 (1966).

127. P. Coyle, Arterial patterns of the rat rhinencephalon and related structures. *Exp Neurol* **49**, 671-690 (1975).

128. H. Kanemitsu *et al.*, Differences in the extent of primary ischemic damage between middle cerebral artery coagulation and intraluminal occlusion models. *J Cereb Blood Flow Metab* **22**, 1196-1204 (2002).

129. W. Hacke *et al.*, 'Malignant' middle cerebral artery territory infarction: clinical course and prognostic signs. *Arch Neurol* **53**, 309-315 (1996).

130. F. Arnberg, J. Lundberg, M. Söderman, P. Damberg, S. Holmin, Image-guided method in the rat for inducing cortical or striatal infarction and for controlling cerebral blood flow under MRI. *Stroke* **43**, 2437-2443 (2012).

131. P. A. Yushkevich *et al.*, User-guided 3D active contour segmentation of anatomical structures: significantly improved efficiency and reliability. *Neuroimage* **31**, 1116-1128 (2006).

132. W. D. Heiss, O. Zaro Weber, Validation of MRI Determination of the Penumbra by PET Measurements in Ischemic Stroke. *J Nucl Med* **58**, 187-193 (2017).

133. M. Wintermark *et al.*, Comparative overview of brain perfusion imaging techniques. *Stroke* **36**, e83-99 (2005).

134. A. C. Silva, W. Zhang, D. S. Williams, A. P. Koretsky, Multi-slice MRI of rat brain perfusion during amphetamine stimulation using arterial spin labeling. *Magn Reson Med* **33**, 209-214 (1995).

135. S. P. Lee, T. Q. Duong, G. Yang, C. Iadecola, S. G. Kim, Relative changes of cerebral arterial and venous blood volumes during increased cerebral blood flow: implications for BOLD fMRI. *Magn Reson Med* **45**, 791-800 (2001).

136. J. Mulder *et al.*, Tissue profiling of the mammalian central nervous system using human antibody-based proteomics. *Mol Cell Proteomics* **8**, 1612-1622 (2009).

137. A. Rayasam *et al.*, Immune responses in stroke: how the immune system contributes to damage and healing after stroke and how this knowledge could be translated to better cures? *Immunology* **154**, 363-376 (2018).

138. E. J. Su *et al.*, Microglial-mediated PDGF-CC activation increases cerebrovascular permeability during ischemic stroke. *Acta Neuropathol* **134**, 585-604 (2017).

139. A. Al Mamun *et al.*, Microglial IRF5-IRF4 regulatory axis regulates neuroinflammation after cerebral ischemia and impacts stroke outcomes. *Proc Natl Acad Sci U S A* **117**, 1742-1752 (2020).

140. T. Brott *et al.*, Measurements of acute cerebral infarction: lesion size by computed tomography. *Stroke* **20**, 871-875 (1989).

141. M. Fisher, B. Bastan, Identifying and utilizing the ischemic penumbra. *Neurology* **79**, S79-85 (2012).

142. M. J. Donahue *et al.*, Consensus statement on current and emerging methods for the diagnosis and evaluation of cerebrovascular disease. *J Cereb Blood Flow Metab*, 271678X17721830 (2017).

143. A. R. Young *et al.*, Relationships between high oxygen extraction fraction in the acute stage and final infarction in reversible middle cerebral artery occlusion: an investigation in anesthetized baboons with positron emission tomography. *J Cereb Blood Flow Metab* **16**, 1176-1188 (1996).

144. T. Temma *et al.*, Estimation of oxygen metabolism in a rat model of permanent ischemia using positron emission tomography with injectable15O-O2. *J Cereb Blood Flow Metab* **26**, 1577-1583 (2006).

145. T. A. Kent *et al.*, Cerebral blood volume in a rat model of ischemia by MR imaging at 4.7 T. *AJNR Am J Neuroradiol* **10**, 335-338 (1989).

146. R. Fern, Ischemia: astrocytes show their sensitive side. *Prog Brain Res* **132**, 405-411 (2001).

147. C. K. Petito, J. P. Olarte, B. Roberts, T. S. Nowak, W. A. Pulsinelli, Selective glial vulnerability following transient global ischemia in rat brain. *J Neuropathol Exp Neurol* **57**, 231-238 (1998).

148. Z. L. Yang, L. J. Zhang, PET/MRI of central nervous system: current status and future perspective. *Eur Radiol* **26**, 3534-3541 (2016).

149. N. Menjot de Champfleur *et al.*, Efficacy of Stent-Retriever Thrombectomy in Magnetic Resonance Imaging Versus Computed Tomographic Perfusion-Selected Patients in SWIFT PRIME Trial (Solitaire FR With the Intention for Thrombectomy as Primary Endovascular Treatment for Acute Ischemic Stroke). *Stroke* **48**, 1560-1566 (2017).

150. M. Rocha, T. G. Jovin, Fast Versus Slow Progressors of Infarct Growth in Large Vessel Occlusion Stroke: Clinical and Research Implications. *Stroke* **48**, 2621-2627 (2017).

151. R. Motyer *et al.*, Endovascular thrombectomy beyond 12 hours of stroke onset: a stroke network's experience of late intervention. *J Neurointerv Surg*, (2018).

152. H. Tsukada *et al.*, PET imaging of ischemia-induced impairment of mitochondrial complex I function in monkey brain. *J Cereb Blood Flow Metab* **34**, 708-714 (2014).

153. A. Martín *et al.*, In vivo PET imaging of the α4β2 nicotinic acetylcholine receptor as a marker for brain inflammation after cerebral ischemia. *J Neurosci* **35**, 5998-6009 (2015).